

RESEARCH ARTICLE

10.1002/2017GB005753

Key Points:

- Nitrate is highly sensitive to biogeochemical model parameterizations and useful for model assessment
- Dynamic biological functioning improves the simulated distribution of major biogeochemical fields in a global ocean model
- Dynamic biological functioning reduces the sensitivity of important fields, like carbon, to physical changes

Supporting Information:

- Supporting Information S1

Correspondence to:

P. J. Buchanan,
pearse.buchanan@utas.edu.au

Citation:

Buchanan, P. J., Matear, R. J., Chase, Z., Phipps, S. J., & Bindoff, N. L. (2018). Dynamic biological functioning important for simulating and stabilizing ocean biogeochemistry. *Global Biogeochemical Cycles*, 32, 565–593. <https://doi.org/10.1002/2017GB005753>

Received 29 JUN 2017

Accepted 14 FEB 2018

Accepted article online 21 FEB 2018

Published online 16 APR 2018

Dynamic Biological Functioning Important for Simulating and Stabilizing Ocean Biogeochemistry

P. J. Buchanan^{1,2,3,4} , R. J. Matear² , Z. Chase¹ , S. J. Phipps^{1,4} , and N. L. Bindoff^{1,3,4} 

¹Institute for Marine and Antarctic Studies, University of Tasmania, Hobart, Tasmania, Australia, ²CSIRO Oceans and Atmosphere, CSIRO Marine Laboratories, Hobart, Tasmania, Australia, ³ARC Centre of Excellence in Climate System Science, University of Tasmania, Hobart, Tasmania, Australia, ⁴Antarctic Climate and Ecosystems Cooperative Research Centre, University of Tasmania, Hobart, Tasmania, Australia

Abstract The biogeochemistry of the ocean exerts a strong influence on the climate by modulating atmospheric greenhouse gases. In turn, ocean biogeochemistry depends on numerous physical and biological processes that change over space and time. Accurately simulating these processes is fundamental for accurately simulating the ocean's role within the climate. However, our simulation of these processes is often simplistic, despite a growing understanding of underlying biological dynamics. Here we explore how new parameterizations of biological processes affect simulated biogeochemical properties in a global ocean model. We combine 6 different physical realizations with 6 different biogeochemical parameterizations (36 unique ocean states). The biogeochemical parameterizations, all previously published, aim to more accurately represent the response of ocean biology to changing physical conditions. We make three major findings. First, oxygen, carbon, alkalinity, and phosphate fields are more sensitive to changes in the ocean's physical state. Only nitrate is more sensitive to changes in biological processes, and we suggest that assessment protocols for ocean biogeochemical models formally include the marine nitrogen cycle to assess their performance. Second, we show that dynamic variations in the production, remineralization, and stoichiometry of organic matter in response to changing environmental conditions benefit the simulation of ocean biogeochemistry. Third, dynamic biological functioning reduces the sensitivity of biogeochemical properties to physical change. Carbon and nitrogen inventories were 50% and 20% less sensitive to physical changes, respectively, in simulations that incorporated dynamic biological functioning. These results highlight the importance of a dynamic biology for ocean properties and climate.

Plain Language Summary The ocean's biogeochemistry is important for controlling concentrations of atmospheric greenhouse gases and therefore plays a key role in climate. An important part of ocean biogeochemistry are the numerous biological processes that occur in the ocean. In this study, we use a number of newly proposed ways to simulate the complex biological processes of the ocean. We find that these formulations provide a number of important improvements when combined. Not only do they allow the ocean model to simulate observed, regional features of ocean biology, but they also improve the simulation of ocean biogeochemistry on a global scale. We uniquely find through changing the biological and physical characteristics of the ocean that the nitrogen cycle is the most responsive to biological change, and we suggest that future assessments of ocean biogeochemical models use nitrate as a primary assessment tool. Finally, we find that including dynamic biological processes reduces the ocean's sensitivity to physical changes. Ocean biology could therefore act as a buffer to the effects of climate change through its response to environmental conditions.

1. Introduction

The ocean is a powerful player in the global climate system. Due to its large volume and surface area, the biogeochemical properties of the ocean are an important control on atmospheric concentrations of carbon dioxide and other greenhouse gases. The biological pump, which involves the fixation of carbon and other elements within organic matter and their subsequent transfer to depth, plays an important role in regulating atmospheric CO₂. There is strong evidence from proxy and model studies that variations in the strength of the biological pump, in conjunction with reorganizations of ocean circulation, played a major role in setting past

climates (Buchanan et al., 2016; Kohfeld et al., 2005; Schmittner & Somes, 2016). The response of the biological pump under anthropogenic climate change will influence the evolution of Earth's climate.

Accurately simulating biological processes in the ocean is therefore fundamental for accurately simulating the behavior of the climate system over millennial time scales. In its broadest sense, the processes that govern the ocean's biological pump can be defined as (1) those that create organic matter from inorganic matter, (2) those that create inorganic matter from organic matter (rem mineralization), and (3) those that control the quantities of elements involved in these exchanges. All three processes can be depicted simply by equation (1), originally given by Redfield (1963).



Here production of organic matter involves the forward reaction, while the rem mineralization of organic matter involves the reverse reaction. The quantities of elements involved are found by balancing the chemical formula and coincide with the Redfield ratio of C:N:P:O₂ as 106:16:1:-138.

A few equations defined in seminal studies from the twentieth century are largely used in ocean biogeochemical models to simulate the biological pump. Nutrient and light availability are commonly used to limit the maximum potential growth rate set by temperature (Eppley, 1972). Typically, the nutrient requirements for phytoplankton growth are based on an unchanging Monod function (Dugdale, 1967; Monod & Wollman, 1947), such that a given phytoplankton type has fixed nutrient requirements. The rem mineralization of organic matter through the water column is commonly parameterized according to a function of depth, often referred to as a Martin curve (Martin et al., 1987), which again is typically fixed for a given phytoplankton type. Finally, the quantities of elements that are involved in the reaction of equation (1) are prescribed according to the Redfield ratio (Fleming, 1940; Redfield, 1963; Redfield et al., 1937), or a variation thereof (Anderson, 1995; Takahashi et al., 1985), and also remain unchanged.

These traditional equations, which are explained more completely in Appendix A, are a rudimentary representation of what is a complex ecological web with biogeochemical consequences (Worden et al., 2015). Modeling studies using the traditional equations (e.g., Buchanan et al., 2016; Joos, 1999; Mariotti et al., 2012; Matear & Hirst, 1999; Sarmiento et al., 1998; Schmittner, 2005; Schmittner & Somes, 2016) are thus compromised by overly simplistic responses to physical changes. However, simulating the biological pump in a more realistic way is challenging, and the community has slowly integrated more complex ecosystem models and processes to improve the simulation of global ocean biogeochemistry (Aumont et al., 2017; Boyd & Doney, 2002; Dutkiewicz et al., 2013; Le Quééré et al., 2016; Weber & Deutsch, 2012). These studies have each demonstrated that simulated biogeochemical fields are improved by including additional biogeochemical complexity, but each has focussed on particular biogeochemical tracers of interest. Simulations that explore the role of the biological pump in a future climate using the current suite of ocean biogeochemical models are therefore difficult to interpret because each represents biological processes in different ways, which may show divergent projections of key properties (see the multimodel analysis by Laufkötter et al., 2016, for an example).

The challenge, therefore, is to include the wider effects of biogeochemical processes using simple, digestible formulations. This challenge is made more difficult by the inability of climate models to reliably reproduce the physical state of the modern and historical ocean. The formation of Antarctic Bottom Water and its properties are poorly represented among climate system models, with dense waters formed via deep convection occurring in the open ocean rather than by buoyancy changes on the Antarctic shelves (Heuzé et al., 2013). Likewise, the northward extension of intermediate waters from the Southern Ocean is limited in models (Sloyan & Kamenskovich, 2007), possibly caused by surface mixing that is too shallow and too far north (Sallée, Shuckburgh, Bruneau, Meijers, Bracegirdle & Wang, 2013), leading to a light and warm bias (Sallée, Shuckburgh, Bruneau, Meijers, Bracegirdle, Wang & Roy, 2013). Unfortunately, many more dynamical inconsistencies are common to global ocean models, which must sacrifice resolution for computational efficiency, and must therefore include the effects of mesoscale and submesoscale dynamics through crude parameterizations (Hallberg, 2013). In addition, our understanding of ocean dynamics in the current climate is also imperfect. Estimates of the modern circulation have undergone multiple revisions over the past few decades, with apparently large ranges in the transport rates of globally important water masses (Talley, 2013; Talley et al., 2003). An imperfect understanding of physical dynamics coupled with an inability to reproduce observed conditions makes it difficult to have confidence in how we simulate biological processes,

particularly as certain biogeochemical tracers like oxygen and carbon appear to be highly sensitive to physical change (Cocco et al., 2013; Marinov et al., 2008; Séférian et al., 2013).

Fortunately, a number of simple parameterizations that mechanistically produce the large-scale features of marine biological communities have been designed for ease of uptake into ocean biogeochemical models. They are improvements on the traditional equations that add flexibility to the limitation of primary production by phosphate and nitrate (Smith et al., 2009), remineralization rates (Marsay et al., 2015; Weber et al., 2016), and stoichiometry (Galbraith & Martiny, 2015). We assess these new parameterizations and their effect on global ocean biogeochemical fields using the ocean component of the Commonwealth Scientific and Industrial Research Organisation Mark 3L (CSIRO Mk3L) Earth system model. In consideration of uncertainty in the physical state of the ocean, we make this assessment using a number of plausible preindustrial physical states and explore the influence of physical and biological processes on ocean biogeochemistry. We find that the dynamic biological functioning produced by these simple formulations in combination is fundamental for simulating and stabilizing ocean biogeochemistry.

2. Experimental Design

To assess the sensitivity of biogeochemical changes to variations in both the physical and biological state of the ocean, we generated six unique physical and biogeochemical model states. Physical states were generated using the Ocean General Circulation Model (OGCM) from within the CSIRO Mk3L (Phipps et al., 2013). Biological states were generated by modifying the ocean biogeochemical model attached to the OGCM. A description of the ocean biogeochemical model is located in Appendix A. A total of 36 experiments were run for 10,000 years toward equilibrium for all physical and biogeochemical fields. In the following we detail how each unique physical and biological state was generated.

2.1. Physical States

Six physical states were generated by forcing the OGCM with six realizations of the preindustrial climate. The OGCM requires monthly climatologies of sea surface temperature ($^{\circ}\text{C}$), sea surface salinity (practical salinity unit), and surface wind stresses (Pa) to calculate surface fluxes and large-scale ocean dynamics. The biogeochemical model requires climatologies of sea ice cover, surface wind speeds, incident short wave radiation, and the aeolian deposition of iron and reactive nitrogen to the surface ocean. With the exception of the aeolian deposition fields, which were provided by Mahowald et al. (2005) for iron and Lamarque et al. (2013) for reactive nitrogen, each physical state was generated using a unique set of surface climatologies. The model interpolates linearly in time between the climatological means for each calendar month.

The preindustrial climatologies for the Mk3L physical state were provided by a 10,000 year spin up of the flux adjusted CSIRO Mk3L coupled climate system model. For the remaining five physical states, surface climatologies were provided by five climate system models from the Climate Model Intercomparison Project phase 5 (CMIP5) multimodel ensemble (Taylor et al., 2012). These models comprise GFDL-ESM2G, IPSL-CM5A-MR, HadGEM2-CC, MPI-ESM-MR, and MRI-CGCM3 (Table 1). As part of the CMIP5 protocol, these groups were required to undertake a multcentury control simulation under preindustrial conditions. The surface fields required to force the OGCM and biogeochemical model were downloaded from the Earth System Grid Federation database (<https://esgf-node.jpl.nasa.gov/projects/esgf-jpl/>), and the months over the final 10 years of the preindustrial run were averaged to provide monthly climatologies. These climatologies were regridded onto CSIRO Mk3L grid space using the *Ferret* program.

Note that the incident shortwave radiation field for HadGEM2-CC was unavailable and was substituted by the net shortwave radiation field of GFDL-ESM2G, which a priori had the most similar sea surface temperature climatology to HadGEM2-CC with an r^2 of 0.98 and a mean bias of $+0.01^{\circ}\text{C}$.

All ocean physical states were therefore generated using the OGCM physics of CSIRO Mk3L but were forced by different surface boundary conditions. We will hereby refer to the six physical states according to the origins of the boundary conditions by which they were forced: Mk3L, Geophysical Fluid Dynamics Laboratory (GFDL), Institut Pierre-Simon Laplace (IPSL), Hadley Centre Global Environmental Model (HadGEM), Max Planck Institute for Meteorology (MPI), and Meteorological Research Institute (MRI) ocean states.

2.2. Biological States

Six unique biological states were generated. Changes to organic matter production, remineralization, and/or the elemental composition (stoichiometry) of the general phytoplankton type were made by implementing

Table 1
A Summary of the Physical and Biological States That Were Produced Within the Ocean Biogeochemical Model

Physical states	Modeling group	Experiment	Variables
1. Mk3L	Commonwealth Scientific and Industrial Research Organisation	(Phipps et al., 2013)	tos, sos, rsntds, tauu, tauv, sfcWind, sic
2. GFDL	NOAA Geophysical Fluid Dynamics Laboratory	piControl	tos, sos, rsntds, tauu, tauv, sfcWind, sic
3. IPSL	Institut Pierre-Simon Laplace	piControl	tos, sos, rsntds, tauu, tauv, sfcWind, sic
4. HadGEM	Met Office Hadley Centre	piControl	tos, sos, tauu, tauv, sfcWind, sic
5. MPI	Max Planck Institute for Meteorology	piControl	tos, sos, rsntds, tauu, tauv, sfcWind, sic
6. MRI	Meteorological Research Institute	piControl	tos, sos, rsntds, tauu, tauv, sfcWind, sic
Biological states	Function	Modification dependencies	Proposed by
1. Base		None	
2. OUK	Nutrient limitation of phytoplankton	NO ₃ and PO ₄	(Smith et al., 2009)
3. Rem _T	Depth of remineralization	Temperature	(Marsay et al., 2015)
4. Rem _P	Depth of remineralization	Picoplankton fraction of community	(Weber et al., 2016)
5. V _{ele}	Elemental composition of organic matter	NO ₃ and PO ₄	(Galbraith & Martiny, 2015)
6. COM	Combination of OUK, Rem _P , and V _{ele}	as above	

Note. Five of the six physical states were generated using surface climatologies produced by the preindustrial control (piControl) run as part of the Climate Model Intercomparison Project phase 5 (CMIP5; Taylor et al., 2012). The surface climatologies used to force the OGCM of CSIRO Mk3L were sea surface temperature (tos), sea surface salinity (sos), surface downward eastward stress (tauu), and surface downward northward stress (tauv). Surface climatologies additionally needed for the biogeochemical model were net downward shortwave flux at sea water surface (rsntds), wind speed (sfcWind), and sea ice area fraction (sic). Each biological state was tested within each of the six physical states, for a total of 36 experiments.

recently proposed formulations that express how marine biology responds to its environment (Galbraith & Martiny, 2015; Marsay et al., 2015; Smith et al., 2009; Weber et al., 2016) (Table 1).

2.2.1. Basic Biogeochemical Model (Base)

The *Base* biogeochemical model used a number of equations defined in seminal studies from the twentieth century to simulate the processes that govern biological production, remineralization, and stoichiometry in the ocean, and these are described in more detail in Appendix A. The *Base* biological state ensured that the nutrient requirements for growth, the rate of remineralization, and the stoichiometry of organic matter were constant everywhere. The *Base* biological state therefore represented a biological community that did not alter its functioning in response to environmental change. In other words, the biogeochemical features of the phytoplankton community did not change.

2.2.2. Variable Nutrient Limitation of Organic Matter Production (Optimal Uptake Kinetics)

The universal application of Michaelis-Menten kinetics to nutrient uptake by phytoplankton is an oversimplification (Flynn, 2003), and optimal uptake kinetics (*OUK*) was developed to express how phytoplankton optimize their nutrient uptake depending on ambient nutrient concentrations (Smith et al., 2009). Essentially, *OUK* captures how different phytoplankton communities respond and grow within different nutrient regimes. It assumes that phytoplankton dynamically alter their internal resources between surface uptake sites, which absorb external nutrients, and internal enzymes, which assimilate the nutrients for growth. By taking this phenomenon into account, Smith et al. (2009) were able to calculate faster growth rates of phytoplankton in oligotrophic waters by assuming that these phytoplankton directed more resources toward surface uptake sites.

To implement *OUK* within CSIRO Mk3L (experiment *OUK*), the fraction of the internal nutrient store that is allocated to either surface uptake sites (f_A) or internal enzymes ($1 - f_A$) was calculated.

$$f_A = \max \left[\left(1 + \sqrt{\frac{[\text{NO}_3]}{0.187}} \right)^{-1}, \left(1 + \sqrt{\frac{[\text{PO}_4] \cdot \text{N:P}}{0.187}} \right)^{-1} \right] \quad (2)$$

The value 0.187 in each term represents the short-term approximation ratio between the maximum uptake rate and the maximum affinity for either nutrient, and its derivation is supplied in the Appendix of

Smith et al. (2009). Once the partitioning of nutrient between internal stores (f_A) was solved, the nutrient limitation terms for PO_4 and NO_3 were calculated

$$\text{PO}_{4\text{lim}}^{\text{OUK}} = \frac{[\text{PO}_4]}{\frac{[\text{PO}_4]}{1-f_A} + \frac{0.187}{f_A \cdot \text{N:P}}} \quad (3)$$

$$\text{NO}_{3\text{lim}}^{\text{OUK}} = \frac{[\text{NO}_3]}{\frac{[\text{NO}_3]}{1-f_A} + \frac{0.187}{f_A}} \quad (4)$$

and applied to the calculation of export production (equation (A5)).

It is important to note that the limitation term for iron (Fe_{lim}) was not altered (equation (A4)). It was unchanged from its Michaelis-Menten formulation with a half-saturation constant (K_{Fe}) equal to $0.1 \mu\text{mol m}^{-3}$. The limitation on growth caused by iron was therefore unchanged across the global ocean.

2.2.3. Temperature-Dependent Remineralization (Rem_T)

Since the Martin curve was proposed, numerous studies have questioned its application within different oceanic environments. Sediment trap measurements have shown large variations in the power law exponent b (Berelson, 2001; Francois et al., 2002), with values commonly ranging from -1.3 to -0.6 . These results have shown that generalizing a common rate of remineralization across the ocean is an oversimplification (Olli, 2015).

Temperature could be an important factor with primary control over the rate of remineralization within the ocean interior. The long-standing relationship between temperature and the growth rate of marine plankton (Eppley, 1972) also extends to heterotrophic bacteria in the ocean interior (Laws et al., 2000). Moreover, there appears to be no evidence for microbial community adaptation to latitudinal temperature differences (Bendtsen et al., 2015). If this is true, then cooler regions of the ocean should support reduced rates of remineralization and therefore allow more organic matter to enter deeper waters (i.e., less negative b values), while warmer regions should have steeper remineralization profiles, where less organic matter enters deeper waters. Strong evidence for a temperature-dependent remineralization rate was demonstrated by Buesseler et al. (2007), who reported that roughly 50% of the organic matter falling from 150 m in subarctic waters was present at 500 m, while only 20% remained at 500 m in the subtropical North Pacific.

To apply a temperature-dependent remineralization rate within CSIRO Mk3L (experiment Rem_T), we altered the b exponent of the Martin curve according to Marsay et al. (2015).

$$b = -(0.062 \cdot T + 0.303) \quad (5)$$

where T is the average temperature ($^{\circ}\text{C}$) of the upper 500 m of the water column.

Marsay et al. (2015) predicted the flux of particulate organic matter into the ocean interior across four sites in the North Atlantic Ocean using this relationship. However, using equation 5 gave values greater than -0.4 across large areas of the high latitudes, as mesopelagic water temperatures are typically less than 2°C . Considering that estimates of the b exponent based on observations have rarely featured values greater than -0.6 (Berelson, 2001; Francois et al., 2002), we applied an upper limit of -0.6 to equation (5).

2.2.4. Phytoplankton-Dependent Remineralization (Rem_p)

Recently, Weber et al. (2016) found that the composition of the phytoplankton community, specifically the component fraction of picoplankton (F_{pico}), was a superior predictor of organic matter transfer into the ocean interior. Using global distributions of nutrient and oxygen tracers along transport pathways, rather than directly measuring organic flux, they found that F_{pico} could explain 93% of the variance in the observations, while temperature could only explain 70%.

Here we used the equation provided by Weber et al. (2016) within CSIRO Mk3L (experiment Rem_p), where the transfer efficiency (T_{eff}) of organic matter from the bottom of the euphotic zone to 1,000 m was determined by

$$T_{\text{eff}} = 0.47 - 0.81 \cdot F_{\text{pico}} \quad (6)$$

Because CSIRO Mk3L does not simulate picoplankton, we estimated F_{pico} for each surface grid using a linear parameterization, where high F_{pico} values are found in regions with low organic carbon production (C_{org}) and $C_{\text{org}}^{\text{max}}$ represents the maximum rate of organic carbon production from the ocean at the previous day.

$$F_{\text{pico}} = 0.51 - 0.26 \cdot \frac{C_{\text{org}}(\text{mg C m}^{-2} \text{ h}^{-1})}{C_{\text{org}}^{\text{max}}(\text{mg C m}^{-2} \text{ h}^{-1})} \quad (7)$$

This simple parameterization is informed by the estimates of F_{pico} reported by Weber et al. (2016), where values of 0.3 were found in highly productive regions and values as high as 0.55 were found in the oligotrophic subtropical gyres. It is also informed by global observations of particle distributions, where picoplankton dominate low productivity regions and microplankton dominate the highly productive regions (Kostadinov et al., 2009). Furthermore, small taxa are observed to dominate Southern Ocean communities during non-bloom conditions (Deppeler & Davidson, 2017), leading to weak organic flux to depth (Ducklow et al., 2015; Weeding & Trull, 2014). A maximum production at the previous day sets $C_{\text{org}}^{\text{max}}$, which allows for similar values of F_{pico} between different ocean states, but alters the spatial patterns. This parameterization also returned T_{eff} values in the range provided by Weber et al. (2016) from 0.05 to 0.3 for subtropical and polar regions, respectively.

When the T_{eff} was known, we solved for the b exponent in the Martin curve using

$$b = \frac{\log(T_{\text{eff}})}{\log\left(\frac{1,000}{100}\right)} = \frac{\log(T_{\text{eff}})}{1} \quad (8)$$

where the depth of the euphotic zone was always 100 m, and the transfer efficiency of organic matter falling out of the euphotic zone is referenced to 1,000 m.

2.2.5. Variable Elemental Ratios (V_{ele})

While the Redfield ratio (Redfield et al., 1937) remains a cornerstone of our understanding of ocean biogeochemistry, there is an increasing support for non-Redfield ratios. Numerous studies that together span the global ocean have reported wide variations in the C:N:P ratios of marine organic matter (supporting information Table S1; Anderson, 1995; Anderson & Sarmiento, 1994; Boulahdid & Minster, 1989; Fraga et al., 1998; Geider & La Roche, 2002; Hedges et al., 2002; Klausmeier et al., 2004; Martin et al., 1987, 2013; Peng & Broecker, 1987; Takahashi et al., 1985; Weber & Deutsch, 2010).

Observed variations in nitrogen and carbon stoichiometry (C:N:P ratios) are now considered to be strongly related to nutrient availability in the surface ocean. Higher C:P and N:P ratios are commonly observed in those regions prone to nutrient limitation, while nutrient-replete regions typically show much lower C:P and N:P ratios (Boulahdid & Minster, 1989; Galbraith & Martiny, 2015; Geider & La Roche, 2002; Klausmeier et al., 2004; Martiny et al., 2013). In an attempt to quantify this relationship, Galbraith and Martiny (2015) built a statistical model to predict P:C and N:C ratios of organic matter across the ocean surface using only PO_4 and NO_3 concentrations.

Using their empirical model, we calculated C:P and N:P ratios in CSIRO Mk3L (experiment V_{ele}):

$$\text{C:P} = \left(\frac{6.9 \cdot [\text{PO}_4] + 6}{1,000} \right)^{-1} \quad (9)$$

$$\text{N:C} = 0.125 + \frac{0.03 \cdot [\text{NO}_3]}{0.32 + [\text{NO}_3]} \quad (10)$$

$$\text{N:P} = \text{C:P} \cdot \text{N:C} \quad (11)$$

We also considered how the requirements for oxic ($\text{O}_{\text{rem}}:\text{P}$) and suboxic ($\text{N}_{\text{den}}:\text{P}$) remineralization were affected by changes in the stoichiometry of organic matter. To calculate the requirements for O_2 and NO_3 for remineralization using equations (A10) and (A11) in Appendix A, we first calculated the amount of hydrogen (H:P) and oxygen (O:P) held within organic matter created at the surface.

The Redfield ratio estimates an $O_{rem}:P$ ratio of $-138:1$ and an $N_{den}:P$ ratio of $-94.4:1$ by assuming that all organic matter is well approximated as a carbohydrate of the form CH_2O (Redfield, 1963). This assumption is tenuous as it greatly overestimates the amount of hydrogen and oxygen in organic matter (Anderson, 1995). However, in the absence of an equation that accounts for variations in the primary biomolecules of organic matter, we continued Redfield's legacy by assuming that all organic matter can be approximated as CH_2O . We therefore calculated the C:N:P ratios according to Galbraith and Martiny (2015), then solved for the quantities of hydrogen and oxygen according to equations (A8) and (A9), and finally solved for the $O_2:P$ and $N_{den}:P$ requirements as per equations (A10) and (A11) in Appendix A.

2.2.6. Combination (COM)

We combined the parameterizations of OUK, Rem_p , and V_{ele} within one biogeochemical model to create the sixth biological state (experiment combination, COM). The Rem_7 experiment was excluded following *a posteriori* analyses detailed in section 4.

3. Analyses

We assessed steady state physical and biogeochemical fields against historical observations to determine both the physical and biogeochemical spread of ocean states that were generated. The physical assessment used annual averages of temperature and salinity (Locarnini et al., 2013; Zweng et al., 2013), mixed-layer depth (de Boyer Montégut et al., 2004), and surface wind speeds (Kalnay et al., 1996). The biogeochemical assessment used three-dimensional fields of dissolved inorganic carbon (DIC), alkalinity (ALK), oxygen (O_2), apparent oxygen utilization (AOU), phosphate (PO_4), and nitrate (NO_3) from the Global Ocean Data Analysis Project (Key et al., 2004) and the World Ocean Atlas (WOA; Garcia, Locarnini, Boyer, Antonov, Baranova et al., 2013; Garcia, Locarnini, Boyer, Antonov, Mishonov et al., 2013). All fields were regridded onto CSIRO Mk3L ocean grid space using the *Ferret* program. Comparisons were made visually and by computing descriptive statistics, which included the correlation coefficient, normalized standard deviation, and normalized bias. Together, these univariate metrics are powerful in assessing overall model skill (Stow et al., 2009).

We extended our physical analysis by calculating the formation rates of important water masses and made direct comparisons with estimates from the literature. The formation rate of Antarctic Bottom Water (AABW) was calculated as the minimum global overturning circulation south of $60^\circ S$ between the surface and 2,000 m. The formation rate of North Atlantic Deep Water (NADW) was calculated as the maximum overturning rate in the North Atlantic Ocean north of $30^\circ N$ and between the surface and 2,000 m. The formation rate of North Pacific Intermediate Water (NPIW) was calculated as the maximum overturning rate in the North Pacific Ocean north of $30^\circ N$ and between the surface and 1,000 m. The subduction/upwelling of Southern Source Intermediate Water (SSIW), composed of both Antarctic Intermediate Water (AAIW) and Subantarctic Mode Water (SAMW), was calculated by determining the locations of isopycnal outcropping and the transports across the mixed layer at these outcropping locations (Appendix B).

To measure differences in the global meridional overturning, we used a quantitative measure of the dominance of the upper and lower cells (U:L). U:L was calculated as the ratio of positive to negative stream function transports (Sv) beneath 500 m for particular ocean basins and the global ocean. The magnitude of transport was ignored, and only the sign of overturning included, so that a U:L equal to 1 meant that the upper and lower overturning cells occupied the same volume of the ocean or ocean basin. U:L values greater (less) than 1 represented circulations dominated by northern (southern) sourced deep waters.

We completed one-way analyses of variance (ANOVA) across physical and biological states to determine the importance of physical and biological changes to the three-dimensional distribution of major biogeochemical fields. F statistics are dimensionless values for biogeochemical fields generated from the ANOVA and represent the ratio of variance between experiments (ocean states) to the variance in space within an experiment (ocean state), normalized by the degrees of freedom. Thus, if the F statistic is greater than 1, the variance between ocean states is greater than the variance within ocean states for a given biogeochemical field. An F statistic of 100 indicates that the variance between ocean states is 100 times the variance within ocean states. To provide some context to the variation that was observed in the biogeochemical fields across the experiments, one-way ANOVAs were also performed on purely physical fields of temperature, salinity, and an O_2 tracer only affected by solubility and mixing ($^{phy}O_2$). We also removed the effect of salinity from the alkalinity tracer by computing the alkalinity normalized by salinity (ALKs) according to Friis (2003).

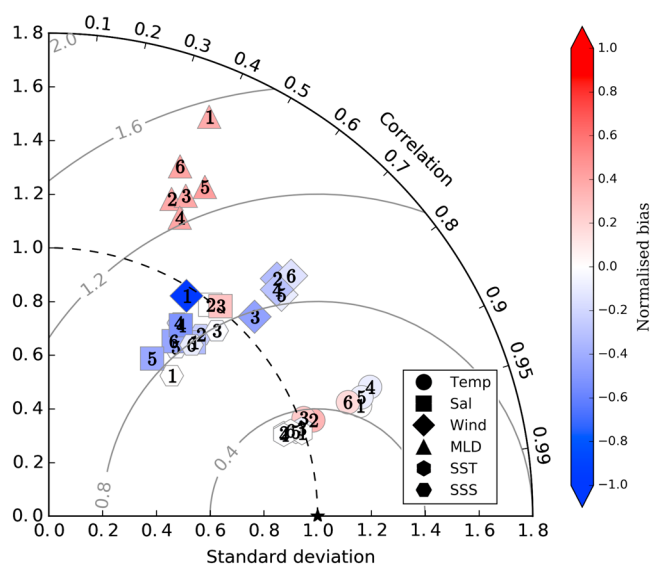


Figure 1. Taylor Diagram (Taylor, 2001) (correlation and normalized standard deviation) with additional color shading (normalized bias) displaying agreement between the simulated and observed fields of temperature (Temp), salinity (Sal), surface winds (Wind), mixed-layer depth (MLD), sea surface temperature (SST), and sea surface salinity (SSS) for all models. Models are represented by numbers: Mark 3L(1), Geophysical Fluid Dynamics Laboratory(2), Institut Pierre-Simon Laplace(3), Hadley Centre Global Environmental Model(4), Max Planck Institute for Meteorology(5), and Meteorological Research Institute(6). Temperature and salinity observations come from the 1955–1964 reconstruction provided by the World Ocean Atlas (Locarnini et al., 2013; Zweng et al., 2013). Surface wind speed observations are the long-term from the National Centers for Environmental Prediction reanalysis of Kalnay et al. (1996). Mixed-layer depth observations are taken from the climatology of de Boyer Montégut et al. (2004). All fields are compared as annual averages.

4. Results

4.1. Physical States

All six physical states showed reasonable agreement in their global fields with observational data sets. Correlations ranged between 0.35 and 0.95 across all fields, and normalized standard deviations did not exceed 150% of the observations (Figure 1). Model-observation agreement was particularly good for the simulated sea surface temperature and whole-ocean temperature fields ($0.93 < r^2 < 0.95$), with some states being over 1°C warmer and others slightly cooler than the historical record (Table 2). Modest agreement was found for the sea surface and whole-ocean salinity fields ($0.55 < r^2 < 0.64$). Again, some states were saltier and others fresher than the historical data. Surface wind speeds were also of modest agreement ($0.53 < r^2 < 0.70$), but all were too weak relative to the National Centers for Environmental Prediction reanalysis data (Kalnay et al., 1996). The poorest model-data agreement was for mixed-layer depths ($0.35 < r^2 < 0.43$), which is a common result among skill assessments of climate models (Séférian et al., 2013). In this suite of experiments, the physical state driven by IPSL surface forcings was most correlated with the observations.

The six physical states formed deep water masses at rates similar to observation-based estimates for the modern ocean (Table 2). The rate of AABW formation, which is a key driver of the lower overturning cell and the properties of the deep ocean, varied from a minimum of 7.2 Sv in GFDL to a maximum of 15.1 Sv in IPSL and MRI. The multimodel mean rate of AABW formation was 12.3 ± 3.0 Sv (mean \pm standard deviation), which is similar to the 12.5 ± 4 Sv estimated by Lumpkin and Speer (2007) for 62°S and an estimate of 14 Sv using chlorofluorocarbons (Orsi et al., 2002). Therefore, all ocean states formed AABW within the range of observational error, with the exception of GFDL.

Table 2

Global Mean Temperature in °C (Locarnini et al., 2013), Global Mean Salinity in Practical Salinity Unit (Zweng et al., 2013), and Estimates of Key Ocean Transports in Sverdrups Taken From the Literature and Those Produced by the Models

	Observations	Mk3L	GFDL	IPSL	HadGEM	MPI	MRI	Model mean + SD
Temp	3.7	4.0	5.4	5.0	3.6	3.6	4.7	4.4 ± 0.7
Sal	34.7	34.5	34.7	34.9	34.4	34.4	34.4	34.6 ± 0.2
AABW ^a	12.5 ± 4	11.5	7.2	15.1	11.4	13.5	15.1	12.3 ± 3.0
NADW ^b	18 ± 5	18.4	20.3	14.8	13.0	16.7	13.9	16.2 ± 2.8
NPIW ^c	2.3 ± 0.1	11.1	11.7	12.7	11.8	12.1	17.2	12.8 ± 2.2
Salinity min	953 m	1148 m	629 m	942 m	856 m	1067 m	1126 m	961 ± 180 m
SSIW sub ^d	11.9	6.5	86.3	3.3	10.2	1.4	1.4	18.2 ± 30.6
SSIW upw ^d	6.1	5.2	108.5	8.1	23.1	6.5	4.0	25.9 ± 37.5

Note. The salinity minimum depth was calculated as the interpolated depth of the salinity minimum at 30°S. See Appendix B for how the values were calculated. All values represent annual averages of the monthly metrics. Bold and italic numbers represent the strongest and weakest rates of circulation, respectively. SD = standard deviation; AABW = Antarctic Bottom Water; NADW = North Atlantic Deep Water; NPIW = North Pacific Intermediate Water; SSIW = Southern Source Intermediate Water; HadGEM = Hadley Centre Global Environmental Model; MPI = Max Planck Institute for Meteorology; MRI = Meteorological Research Institute; Mk3L = Mark 3L; IPSL = Institut Pierre-Simon Laplace; GFDL = Geophysical Fluid Dynamics Laboratory.

^aEstimates from Lumpkin and Speer (2007) with the 14 Sv estimated by Orsi et al. (2002) falling within this range. ^bEstimates from Talley et al. (2003) with the 17 ± 4.3 and 16 ± 2 Sv of Lumpkin and Speer (2007) and Ganachaud (2003) falling within this range. ^cEstimates from Lumpkin and Speer (2007) and Talley et al. (2003). ^dCombined subduction (sub) and upwelling (upw) of AAIW and SAMW from Iudicone et al. (2011).

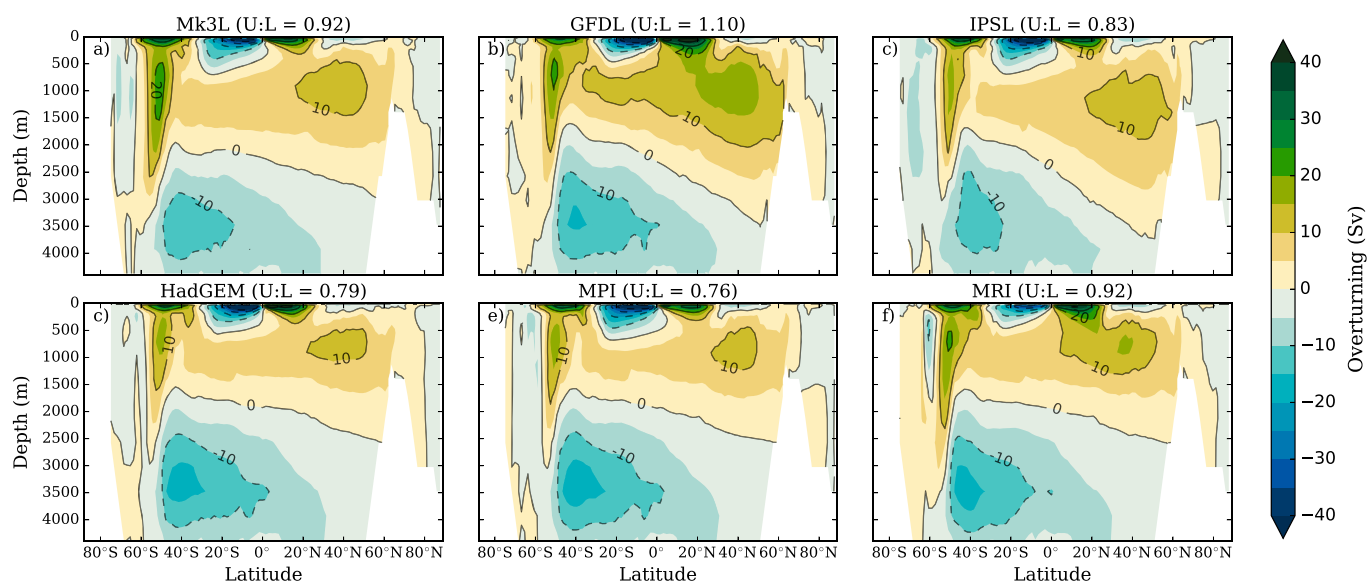


Figure 2. The annual and zonal average of the global meridional overturning circulation for (a–f) all six physical states. U:L represents the dominance of the upper overturning cell relative to the lower overturning cell, calculated by dividing the total area of positive velocities (Sv) by the total area of negative velocities (Sv) beneath 500 m. Note the stronger positive velocities in the upper overturning of MRI caused by greater formation rates of North Pacific Intermediate Water. HadGEM = Hadley Centre Global Environmental Model; MPI = Max Planck Institute for Meteorology; MRI = Meteorological Research Institute; GFDL = Geophysical Fluid Dynamics Laboratory; IPSL = Institut Pierre-Simon Laplace.

The production of NADW, which powers the upper overturning cell, also agreed with observational estimates. GFDL produced the strongest rate of NADW formation at 20.3 Sv, in contrast to its slow rate of AABW formation. The weakest rates of NADW formation were present in HadGEM and MRI at 13.0 and 13.9 Sv, respectively. The range of 13.0–20.3 Sv produced by the six ocean states agrees with the observational error of about 18 ± 5 Sv (Talley et al., 2003), within which other estimates are accounted for (Ganachaud, 2003; Lumpkin & Speer, 2007).

The circulations of intermediate waters, however, showed some striking inconsistencies with observations. Simulated formation rates of NPIW were much greater than observations of ~ 2.3 Sv (Lumpkin & Speer, 2007; Talley et al., 2003). Hence, the ventilation of the North Pacific interior was too great for all states, especially MRI. Meanwhile in the Southern Hemisphere, the combined overturning of SSIW was highly variable in its rate and location. Rapid overturning in excess of 20 Sv at shallow depths were found in HadGEM and GFDL, particularly GFDL, while less than 10 Sv of overturning associated with deeper salinity minima, more consistent with observations (Iudicone et al., 2011), were found in Mk3L, IPSL, MPI, and MRI states (Table 2). Of these, the Mk3L ocean state was the only state to produce net subduction of SSIW. The isopycnals associated with SSIW for these slower rates largely outcropped near the Antarctic coastline, despite deep convective mixing taking place in sub-Antarctic latitudes for all states. Thus, no single ocean state developed NPIW or SSIW dynamics consistent with observations, although some were less inconsistent than others.

The differences in water mass formation (explored more thoroughly in the supporting information; Text S2 and Figures S1 and S2) were responsible for producing the different circulations evident in the global overturning stream function (Figure 2). The ratio of extent of the upper to lower overturning cells (U:L) reflected the major differences between the physical states. GFDL ocean state was strongly dominated by the upper overturning cell (U:L = 1.10) owing to very strong NADW production that drove a stronger Atlantic Meridional Overturning Circulation (AMOC) with an $U:L_{Atl}$ equal to 1.36. In contrast, HadGEM and MPI ocean states were dominated by the lower overturning cell (U:L < 0.80), owing to a stronger and more extensive AABW production relative to NADW production. Mk3L and IPSL ocean states both produced strong AMOCs, but their U:L values were reduced due to the dominance of the lower cells in the Indian and/or Pacific Oceans. This was particularly true of IPSL, for which the influence of a strong AMOC ($U:L_{Atl} = 1.66$) was dampened by a Pacific Ocean dominated by the lower cell. Finally, MRI was unique due to strong NPIW production. The MRI state was clearly dominated by the lower overturning cell in the Indian and Atlantic Oceans ($U:L_{Atl} = 0.91$), but high rates of NPIW formation expanded the upper cell in the Pacific and increased the global U:L value to 0.92.

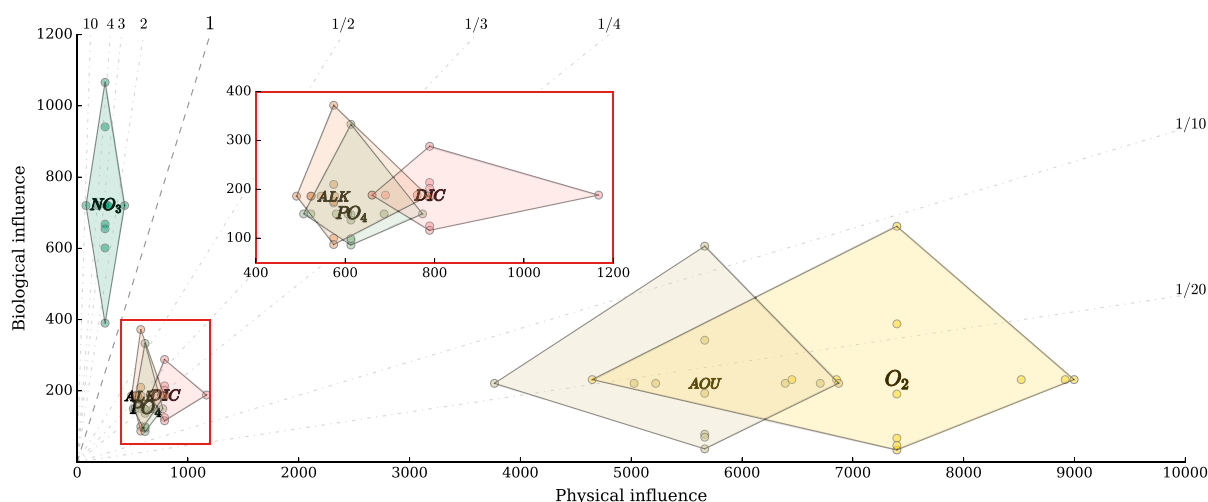


Figure 3. The relative influence of biological versus physical ocean states on major biogeochemical fields. Those fields with a slope < 1 are those more sensitive to changes in physical conditions than biological function, and the steepness of the slope indicates the magnitude of sensitivity in either direction. The measure of influence is quantified as the *F* statistic, which was produced by a ANOVA across the full contingent of physical and biological states in this study. Thus, there are six data points (*F* statistics) for each biogeochemical field in both the physical (*x* axis) and biological (*y* axis) space. The six data points along *x* axis, for instance, represent the *F* statistic values that were generated by conducting ANOVA across all physical states for each biological state, while the six data points along the *y* axis represent the *F* statistic values that were generated across all biological states (Base, OUK, Rem_T, Rem_p, V_{ele}, and COM) for each physical state. All *F* statistic values were highly significant (*p* value < 0.005). DIC = dissolved inorganic carbon; ALK = alkalinity.

Our analysis of the ocean temperature and salinity fields shows a high level of agreement, while a lower level of agreement (albeit still relatively high) was found for other surface boundary conditions (Figure 1). The overturning of important water masses showed a wide range of rates that were broadly consistent for deep waters and less so for intermediate waters. Global thermodynamic states and overturning were therefore plausibly representative of preindustrial conditions in the context of Holocene climate variability (Bond et al., 1997; Mayewski et al., 2004; Rasmussen et al., 2002), while subduction of intermediate waters was too weak in the Southern Ocean and too strong in the North Pacific.

4.2. Physical and Biological State Influence

One-way ANOVA of the major biogeochemical fields quantified how differences in physical and biological states affected their distributions. *F* statistics ranged between 25 and ~9,000 across the physical states and between 34 and 1,066 across the biological states (supporting information Table S2). The variance of each biogeochemical field was significantly different between experiments (*p* values < 0.005). To provide some context for the variation in biogeochemical fields, an ANOVA of purely physical fields showed a range of 320–2,582, with the least variability in temperature and the most in the salinity field. Because these fields were prescribed through a fixed surface climatology, this range represents the variation caused by physical differences. Additionally, the ^{phy}O₂ field produced an *F* statistic of 816, which set a benchmark for changes caused solely by air-sea gas exchange and circulation. Ocean biogeochemistry was generally more sensitive to the physical state of the ocean than to changes in biological function. However, this sensitivity was dependent on the biogeochemical field in question.

O₂ and AOU clearly showed the greatest sensitivity, with at least tenfold the sensitivity to changes in the physical state than to changes in biological functioning (Figure 3). AOU was strongly influenced by physical conditions because of its primary dependence on the circulation (residence time of water masses). Furthermore, O₂ and AOU showed a much greater range of variability under different physical states than the physical states themselves, including ^{phy}O₂. This highlights how changes in the physical state also altered biological function, which had a multiplicative effect on oxygen values.

The carbon species (DIC and ALK) showed less sensitivity to the physical state than oxygen species but still registered a stronger dependence on physical conditions relative to biological function. Of DIC and ALK, the distribution of DIC was more sensitive to the physical state due to physical differences in ocean-atmosphere exchange of CO₂. The variability in the alkalinity field across physical states was shown to be mostly a function of salinity, as the salinity-normalized alkalinity field (ALKs) showed very low *F* statistics (25–38).

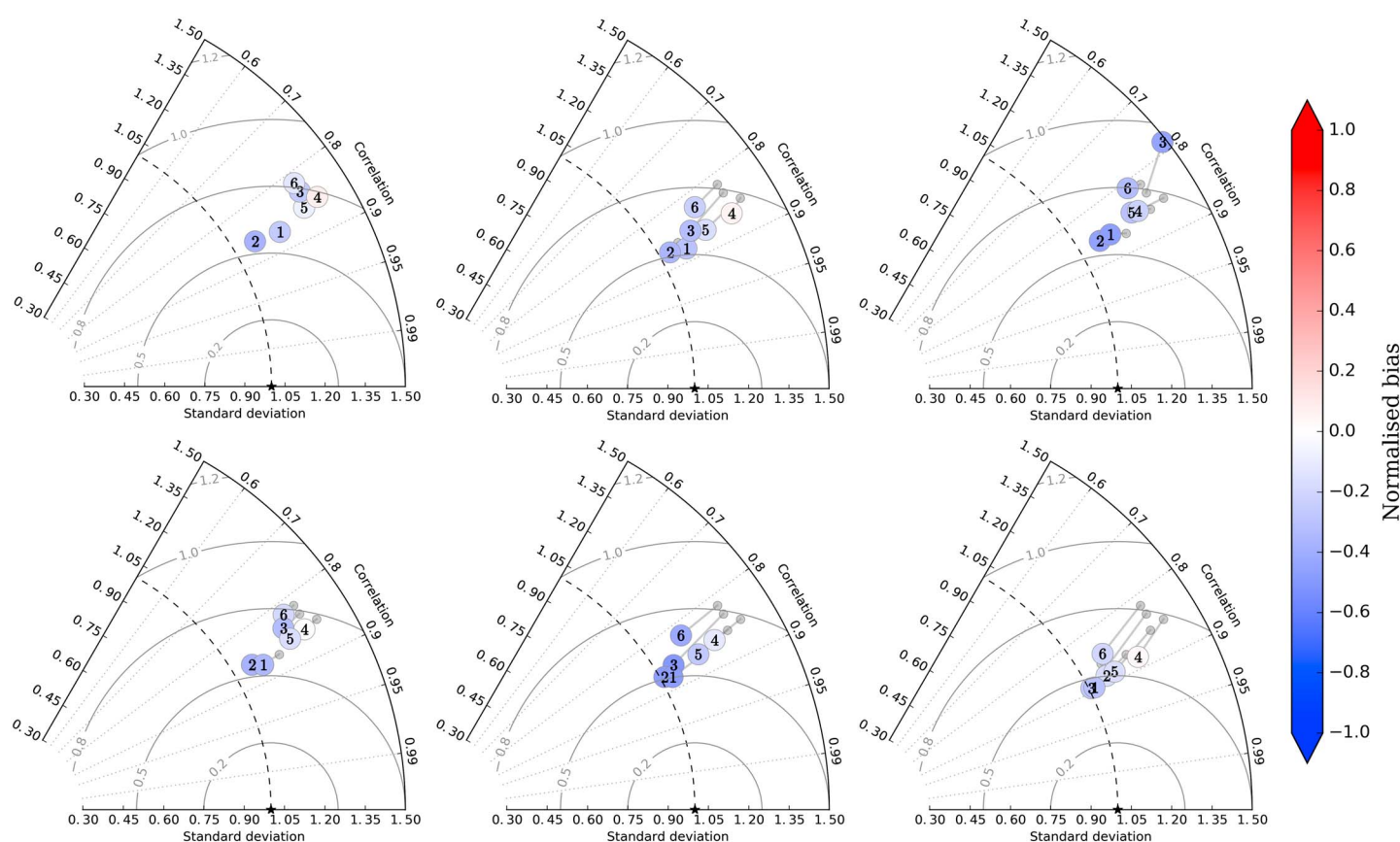


Figure 4. Taylor diagram (Taylor, 2001) displaying agreement between the simulated and observed nitrate field. The Taylor diagram depicts the correlation (angle), normalized standard deviation (radial distance from dashed line), and centered root-mean-square error (outward distance from reference star) between the simulated and observed fields. The small grey circles represent the Base biological state, and the grey line shows the change caused by the new biological state. Additional color shading to represent the normalized bias has been added. For reference, the standard deviation of the observed nitrate field was 9.4 mmol m^{-3} . Observed nitrate data for which the simulated fields are compared to come from the World Ocean Atlas (Garcia, Locarnini, Boyer, Antonov, Baranova et al., 2013). All fields are compared as annual averages.

PO_4 and NO_3 showed contrasting responses to physical and biological state changes, as PO_4 was more sensitive to physical change while NO_3 was more sensitive to biological change. PO_4 was roughly 2 to 4 times more sensitive to differences in physical conditions than in biological functioning. PO_4 showed very low sensitivity (F statistics ≤ 333) to changes in biological function across the physical states. The distribution of NO_3 , however, was approximately 2 to 4 times more sensitive to changes in biological functioning than to changes in the physical state. NO_3 was the only biogeochemical field to be more strongly influenced by the biological state of the ocean than by physical conditions (Figure 3), and this apparent insensitivity occurred despite a wide spread of physical conditions (section 4.1).

4.3. Biological State Assessment

The biological state of the ocean had more influence over the distribution of NO_3 than changes in the physical state, making NO_3 unique. Changes to NO_3 therefore provided the clearest insight into which biological state was most representative of reality. Here we used the marine nitrogen cycle as the primary diagnostic with which to assess the performance of the different biological states.

4.3.1. Base

The biological pump in the Base experiments functioned in the same way globally and was unable to respond dynamically to changes in its environment. The general phytoplankton class functioned as if the same microbial community existed throughout the ocean. This simplistic representation produced reasonable model-observation agreement in the NO_3 field and other oceanic nitrogen cycle diagnostics (Figure 4 and Table 3). Correlations between simulated and observed NO_3 values for the global ocean exceeded 0.8

Table 3
Key Diagnostics of the Oceanic Nitrogen Cycle and Biological Pump for All Biological States Described in Section 2.2 Relative to the Observations for the Modern Ocean

Source	C_{exp}	N_2 fixation	Denitrification	Nitrate			b	N:P	$NO_3:PO_4$	Nitrate			
	(Pg C yr ⁻¹)	(Tg N yr ⁻¹)	(Tg N yr ⁻¹)	(mmol m ⁻³)				(organic)	(nutrient)	r^2	RMSE	SD	
	global	global	global	Global	Surface	Upper	Deep	global	global	> 500 m	global	global	global
Base	7.3 (6.7–8.1)	119 (88–157)	130 (99–168)	29.2	4.9	22.4	36.7	0.858	16.0	14.7 (14.0–15.8)	0.85	8.8	11.5
OUK	7.1 (6.6–7.9)	123 (90–155)	134 (102–166)	28.8	5.4	22.7	35.5	–0.858	16.0	14.4 (13.8–15.6)	0.86	8.0	10.7
Rem _T	7.9 (7.3–8.8)	136 (109–168)	147 (120–180)	27.4	4.2	20.4	35.0	–1.144	16.0	13.7 (13.2–14.3)	0.84	8.4	11.3
Rem _p	7.7 (7.0–8.2)	124 (96–154)	135 (107–165)	28.6	4.9	22.1	35.8	–1.065	16.0	14.3 (13.7–15.3)	0.85	8.2	11.0
V _{ele}	7.1 (6.4–7.7)	120 (92–133)	132 (104–145)	27.3	5.0	21.6	33.6	–0.858	16.9 (15.5–18.1)	14.0 (13.2–15.2)	0.86	7.4	10.3
COM	7.7 (7.5–8.5)	95 (73–106)	106 (85–117)	29.2	6.9	24.5	34.3	–1.057	16.7 (15.7–17.8)	14.6 (14.0–15.6)	0.88	7.6	10.1
Obs	5.1–13	70–175	104–188	30.75	5.2	28.9	32.4	-	-	14.5	1.0	0.0	9.3

Note. Values are the mean across the six physical ocean states and the range in parentheses. C_{exp} refers to the annual export of particulate carbon from the surface and includes general phytoplankton, calcifying plankton, and nitrogen fixers. b refers to the exponent used to set the steepness of the remineralization profile, otherwise known as a Martin curve (Martin et al., 1987). N:P is the stoichiometry of organic matter. $NO_3:PO_4$ is the ratio of water column nitrate to phosphate. The global inventory of phosphate was 2.68 Pmol in all simulations. Observed nitrate concentrations and the $NO_3:PO_4$ ratio of the interior ocean come from the World Ocean Atlas database (Garcia, Locarnini, Boyer, Antonov, Baranova et al., 2013). Observed rates of global denitrification are the range of estimates from Eugster and Gruber (2012). Observed rates of global carbon export production were generated by converting net primary production over the period 2003–2013 produced by the algorithms of Behrenfeld and Falkowski (1997) and Westberry et al. (2008) to carbon export from the euphotic zone using three independent conversions (Dunne et al., 2005; Henson et al., 2011; Laws et al., 2000). RMSE = root-mean-square error; SD = standard deviation.

for all physical states, with a multimodel mean of 0.85. Furthermore, the skill of the physical state was not a good predictor of its ability to simulate NO_3 , with the GFDL state producing the best NO_3 field.

However, a number of inconsistencies between the simulated and observed NO_3 fields were clearly present. Concentrations of NO_3 were underestimated in the upper ocean above 2,000 m by between 5 and 8 mmol m⁻³ on average (Figure 5). In the deep ocean below 2,000 m, NO_3 was overestimated by between 1 and 7 mmol m⁻³ on average, with the lower bound produced by GFDL, which had a very weak lower overturning cell. The error in the vertical distribution of NO_3 was found in all physical states, irrespective of circulation differences.

4.3.2. OUK

The implementation of optimal uptake kinetics (OUK) provided a consistent benefit to the NO_3 field by shifting NO_3 from the deep to the upper ocean (Figure 5). The key tenet of optimal uptake kinetics is that phytoplankton adapt their internal physiology according to the availability of nutrients, reducing efficiency under nutrient-replete (eutrophic) conditions and increasing efficiency under nutrient-deplete (oligotrophic) conditions (Smith et al., 2009). Nutrient utilization in eutrophic regions decreased and delivered more NO_3 to oligotrophic regions, particularly from the subantarctic zone. This shifted nutrients from the deep to the upper ocean and partially rectified the systematic underestimation of upper ocean nutrients. The vertical shift was associated not only with roughly 0.6 mmol m⁻³ increase in the average concentration of NO_3 at the surface but also with a slight increase in the rate of denitrification that caused a global loss of ~0.4 mmol m⁻³. While the loss of NO_3 exacerbated the global negative bias, the change in distribution was beneficial across all physical states (Figure 4).

4.3.3. Rem_T and Rem_p

The introduction of spatial variations in organic matter remineralization also caused global shifts in NO_3 . However, the use of either temperature or phytoplankton-dependent parameterizations to control the remineralization profile (supporting information Figure S3) produced contrasting results.

The use of mesopelagic temperature to control remineralization (Rem_T) was detrimental. It increased the transfer of organics to depth in the high latitudes while simultaneously increasing the recycling of organics in the warm, low-latitude ocean. Approximately 12% more organic matter passed from the surface to 1,000 m depth in the Southern Ocean and Arctic, and this released large quantities of NO_3 into the deep ocean. Meanwhile, warmer temperatures in the lower latitudes produced shallower remineralization profiles, which increased export production (C_{exp}) by about 0.6 Pg C yr⁻¹ and the retention of NO_3 within the mesopelagic zone. Nutrients were therefore more efficiently recycled within the upper 500 m of the ocean, which increased global denitrification by ~18 Tg N yr⁻¹ and lead to a global loss of ~2 mmol NO_3 m⁻³ (Table 3). The loss of NO_3

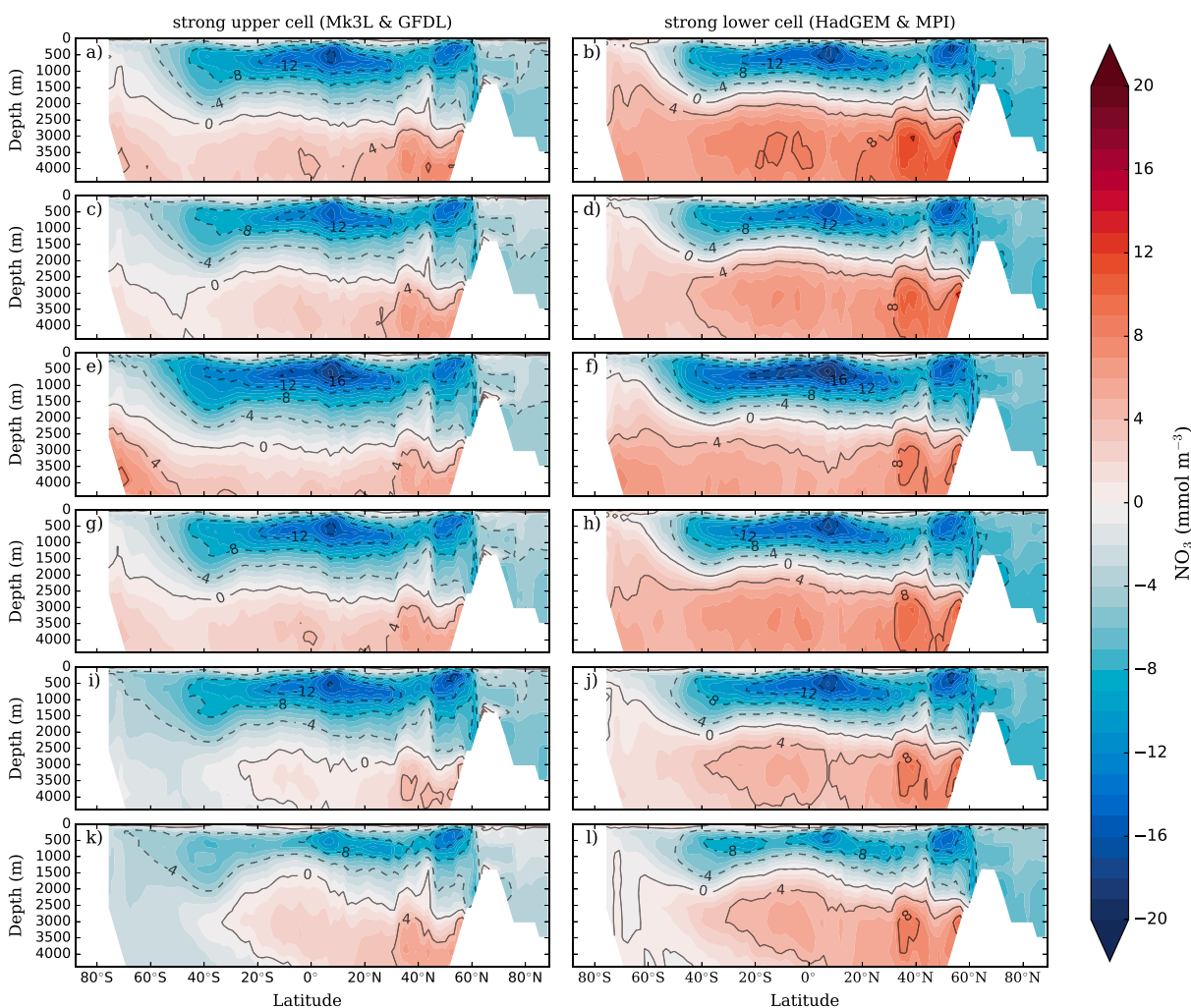


Figure 5. The zonal mean difference between the simulated and observed distributions of NO_3 (mmol m^{-3}) for all biological state experiments. The model-observation difference in NO_3 is shown for two contrasting ocean circulation types. The (a, c, e, g, i, k) strong upper cell is the combined average of GFDL and Mk3L NO_3 fields. The (b, d, f, h, j, l) strong lower cell is the combined average of HadGEM and MPI NO_3 fields. Figures 5a and 5b = Base experiments. Figures 5c and 5d = OUK experiments. Figures 5e and 5f = Rem_7 experiments. Figures 5g and 5h = Rem_p experiments. Figures 5i and 5j = V_{ele} experiments. Figures 5k and 5l = COM experiments.

lowered the interior $\text{NO}_3:\text{PO}_4$ ratio from 14.7:1 to 13.7:1 well below observations of 14.5:1 (Garcia, Locarnini, Boyer, Antonov, Baranova et al., 2013). The combination of very deep remineralization profiles in the high latitudes with efficient nutrient recycling in the low latitudes largely exacerbated the initial biases (Figure 5).

In contrast, phytoplankton-dependent remineralization (Rem_p) slightly improved the simulated NO_3 field by shifting material from the deep to the upper ocean (Figure 5). The shift featured particularly in the Northern Hemisphere and occurred primarily because remineralization profiles shoaled relative to the Base experiments. The global average b exponent varied between -1.06 and -1.08 among the Rem_p experiments, retaining $\sim 4\%$ more organic matter within the upper 1,000 m compared to the -0.87 of the Base experiments (Martin et al., 1987). Because this increased the retention of nutrients at shallower depths, C_{exp} increased by roughly 0.4 Pg C yr^{-1} (Table 3). These changes caused a slight increase in denitrification rates. However, because the transfer of organics to depth in the equatorial zones was deep ($b > -0.8$), local export production decreased and dampened the global increase in denitrification. Global NO_3 concentrations were reduced only slightly (0.5 mmol m^{-3}), and the interior ocean $\text{NO}_3:\text{PO}_4$ ratio remained close to observations at 14.3:1.

4.3.4. V_{ele}

Variable stoichiometry of organic matter (V_{ele}) altered the global distribution of NO_3 by altering the requirements for organic matter production (N:P) and denitrification ($\text{N}_{\text{den}}:\text{P}$). The global average N:P ratio was slightly

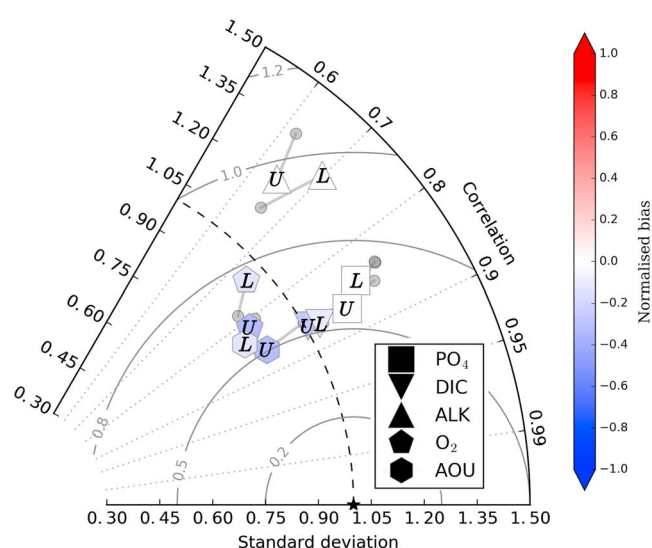


Figure 6. Taylor diagram (Taylor, 2001) displaying agreement between the simulated and observed fields of phosphate (PO_4), dissolved inorganic carbon (DIC), alkalinity (ALK), dissolved oxygen (O_2), and apparent oxygen utilization (AOU). Simulated fields include the mean of Mk3L and IPSL oceans, which have a strong upper overturning cell (U), and the mean of HadGEM and MPI, which have a strong lower overturning cell (L). GFDL and MRI ocean states were excluded because they formed important water masses outside of observational uncertainties (see section 4.1). The Taylor diagram depicts the correlation (angle), normalized standard deviation (radial distance from dashed line), and centered root-mean-square error (outward distance from reference star) between the simulated and observed fields. The small grey circles represent the Base biological state, and the grey line shows the change caused by the new biological state. Additional color shading to represent positive or negative changes in normalized bias due to the COM biological state has been added. For reference, the standard deviations of observations (mmol m^{-3}) are $\text{PO}_4 = 0.68$, $\text{DIC} = 91.4$, $\text{ALK} = 43.0$, $\text{O}_2 = 64.7$, and $\text{AOU} = 67.4$. Nutrient and oxygen observations come from the World Ocean Atlas (Garcia, Locarnini, Boyer, Antonov, Mishonov et al., 2013; Garcia, Locarnini, Boyer, Antonov, Baranova et al., 2013), and carbon data come from the Global Ocean Data Analysis Project (Key et al., 2004). All fields are compared as annual averages.

4.3.5. COM

The COM biological state provided the best simulated-observed agreement in the NO_3 field. Correlations were the highest with a mean of 0.88, standard deviations were brought much closer to observations, and the root-mean-square error was minimized to less than 0.6 standard deviations (Table 3).

The combination of OUK, Rem_p , and V_{ele} produced contrasting responses between eutrophic and oligotrophic environments that allowed NO_3 to shift from the deep to the upper ocean without incurring a loss in the NO_3 inventory (Figure 5). In eutrophic regions, OUK and V_{ele} weakened export production, Rem_p subsequently produced shallower remineralization profiles, and NO_3 was shifted into the upper ocean. In V_{ele} , this shift caused a large loss of NO_3 as low N:P ratios over the Southern Ocean allowed more NO_3 to cycle within denitrification zones (supporting information Figure S4). In COM, however, OUK and Rem_p further lowered $N_{\text{den}}:P$ ratios in the lower latitudes, which reduced denitrification rates. The transfer of NO_3 from the deep to the upper ocean therefore did not incur large global losses in NO_3 , and denitrification was reduced by $\sim 24 \text{ Tg N yr}^{-1}$. Meanwhile in the oligotrophic oceans, higher N:P ratios, stronger production and deeper remineralization profiles ensured that NO_3 was consumed and that nitrogen fixation was maintained. Together, these effects simultaneously shifted NO_3 from the deep to the upper ocean, conserved the global inventory of NO_3 , and produced an interior $\text{NO}_3:\text{PO}_4$ ratio of 14.6:1 that closely approximated the observed 14.5:1 (Table 3).

raised relative to the Redfield ratio of 16:1 for most of the V_{ele} experiments, giving a multimodel average of 16.9:1 (Table 3). Regionally, N:P ratios were lowest in the Southern Ocean (8:1) and in other eutrophic regions, while oligotrophic waters, particularly the North Atlantic and Northern Indian Oceans, were highest (25:1). Likewise, $N_{\text{den}}:P$ ratios were lowered from 94.4 to 70–80 mmol m^{-3} in eutrophic regions, such as the Eastern Equatorial Pacific, but increased within suboxic zones that were overlain with nutrient-deplete waters (supporting information Figure S4).

These large-scale variations in N:P and $N_{\text{den}}:P$ improved the NO_3 distribution for all physical states (Figure 4) and did so for two reasons. First, the NO_3 inventory of the lower overturning cell was strongly reduced, which rectified the overestimation of NO_3 in the deep ocean. The loss of NO_3 from the lower overturning cell was caused by low N:P ratios in the Southern Ocean. Low NO_3 uptake by Southern Ocean phytoplankton reduced the local export of nitrogen to depth, which allowed more NO_3 to exit the lower overturning cell via southern source intermediate waters. The result was a continued loss of the NO_3 from the lower overturning cell to the upper overturning cell.

Second, the loss from the deep ocean was not accompanied by a loss from the upper ocean, which remained relatively unchanged in NO_3 content. The conservation of NO_3 was related to lower $N_{\text{den}}:P$ ratios that reduced denitrification rates. In the Eastern Equatorial Pacific, more NO_3 upwelled to the surface due to low denitrification rates. This enforced a positive feedback mechanism, whereby low N:P ratios at the surface decreased $N_{\text{den}}:P$ ratios, and in turn increased NO_3 delivery to the surface, which further lowered N:P ratios. These changes accumulated NO_3 within the upper Pacific Ocean.

However, low Southern Ocean N:P ratios caused significant losses in the oceanic NO_3 reservoir of 25 to 50 Pg N ($1.4\text{--}2.8 \text{ mmol m}^{-3}$), leading to a consistent negative bias. This loss occurred because more NO_3 was allowed to exit the lower cell and subsequently cycled through denitrification zones. Interestingly, lower NO_3 reservoirs developed despite mean N:P ratios that largely exceeded the Redfield ratio (Table 3), which demonstrated the importance of the lower cell for nutrient storage. The consequence was a detrimental change in the $\text{NO}_3:\text{PO}_4$ ratio of the interior ocean from approximately 14.7:1 in the *Base* experiments to $\sim 13.9:1$.

4.4. Other Biogeochemical Fields

The COM biological state provided the greatest benefit to NO_3 , and we tested its effect on other major biogeochemical fields. For this we placed more importance on the PO_4 , DIC, and ALK fields, as these fields showed a lesser sensitivity to physical changes than O_2 and AOU (Figure 3). Improvements in PO_4 were particularly telling of improvements in the biogeochemical model because this field had no external sources or sinks to or from the ocean.

COM improved the simulated fields of PO_4 , DIC, and ALK in those oceans with a stronger upper cell, while also providing slight improvements to PO_4 and DIC for oceans with a strong lower cell (Figure 6). These fields were improved in their correlation, normalized standard deviation, and/or root-mean-square error relative to the observations provided by WOA and Global Ocean Data Analysis Project data sets (Garcia, Locarnini, Boyer, Antonov, Baranova et al., 2013; Garcia, Locarnini, Boyer, Antonov, Mishonov et al., 2013; Key et al., 2004). The distributions of PO_4 , DIC, and ALK showed the greatest improvement in strong upper cell oceans, while improvements to ALK and oxygen species (O_2 and AOU) were small or even negative for the oceans with a stronger lower cell (HadGEM and MPI). Importantly, the PO_4 and DIC fields showed consistent improvement for both circulation types.

The improvements in PO_4 and DIC mirrored those of NO_3 , as material shifted from the deep to the upper ocean (supporting information Figure S5). This reduced the bias between the simulated and observed values, particularly for oceans with the stronger upper cell, which were oceans that better fit the observed physical fields (see section 4.1). PO_4 and DIC were relocated from the deep ocean into the upper ocean as greater quantities of these species left the lower overturning circulation via the same mechanisms as NO_3 . For DIC, the shift of material into the upper ocean increased the loss of carbon via air-sea gas exchange, and between 125 and 400 Pg C was lost depending on the physical state. This loss rectified the initial overestimation in the deep ocean but did little to resolve an underestimation of DIC in the upper ocean. Overall, however, the COM biological state gave a consistent improvement in the PO_4 and DIC fields across a range of physical states.

4.5. Response of the Carbon and Nitrogen Cycles

Consistent improvement in the simulated-observed agreement for NO_3 , PO_4 , DIC, and ALK provided evidence that COM best represented the functioning of the marine biological community. We therefore evaluated the sensitivity of improved carbon and nitrogen cycles to variation in the ocean's physical state.

The COM biological state reduced differences in global carbon export between the physical states by roughly 0.4 Pg C yr^{-1} (Table 3) and reduced differences in global carbon content between physical states by $\sim 50\%$ (Figure 7). These changes occurred via an interaction between nutrient delivery to the surface and the stoichiometry of organic matter. Those oceans with a weaker AMOC ($U:L_{\text{Atl}} \leq 1.0$), which included HadGEM, MPI, and MRI ocean states, had weaker global rates of export production under the Base biological state. Under the COM biological state, however, more nutrients were delivered to surface waters, which increased biological consumption of PO_4 , increased local C:P ratios through V_{ele} , and further enhanced carbon export. The degree of nutrient limitation in a given physical state was proportional to the increase in global C:P ratios (Figure 7), and this relationship minimized the multimodel spread in biological carbon sequestration. Losses of DIC from all physical states due to the shift of material into the upper ocean, coupled with lower C:P ratios over deep water formation regions, also contributed to greater similarity. Losses occurred in every major oceanic basin, but those oceans with higher C:P ratios (stratified oceans) limited carbon outgassing. As a result of these changes, the range in oceanic carbon inventories halved from 616 Pg C in the Base biological state to 327 Pg C in the COM biological state. In fact, all physical states held roughly 34,000–34,100 Pg C, with the exception of the $\sim 33,800 \text{ Pg C}$ contained within MRI, which reflected reduced storage capacity in the North Pacific due to strong seasonal ventilation by NPIW (see section 4.1).

The similarity in the distribution and inventory of NO_3 increased by $\sim 20\%$ across physical states (Figure 8). In other words, the effect of physical differences was reduced. Under the Base biological state, the circulation of the ocean had a much greater influence on the marine nitrogen cycle, and the total NO_3 inventory could be predicted by scaling the global denitrification rate by the ratio of upper to lower overturning cells (U:L). This simple relationship was due to a relatively deep remineralization profile and a N:P ratio of 16 over the Southern Ocean. NO_3 therefore increased proportionally with the strength of the lower overturning cell. These oceans also tended to be well oxygenated, which reduced global denitrification rates and increased NO_3 storage.

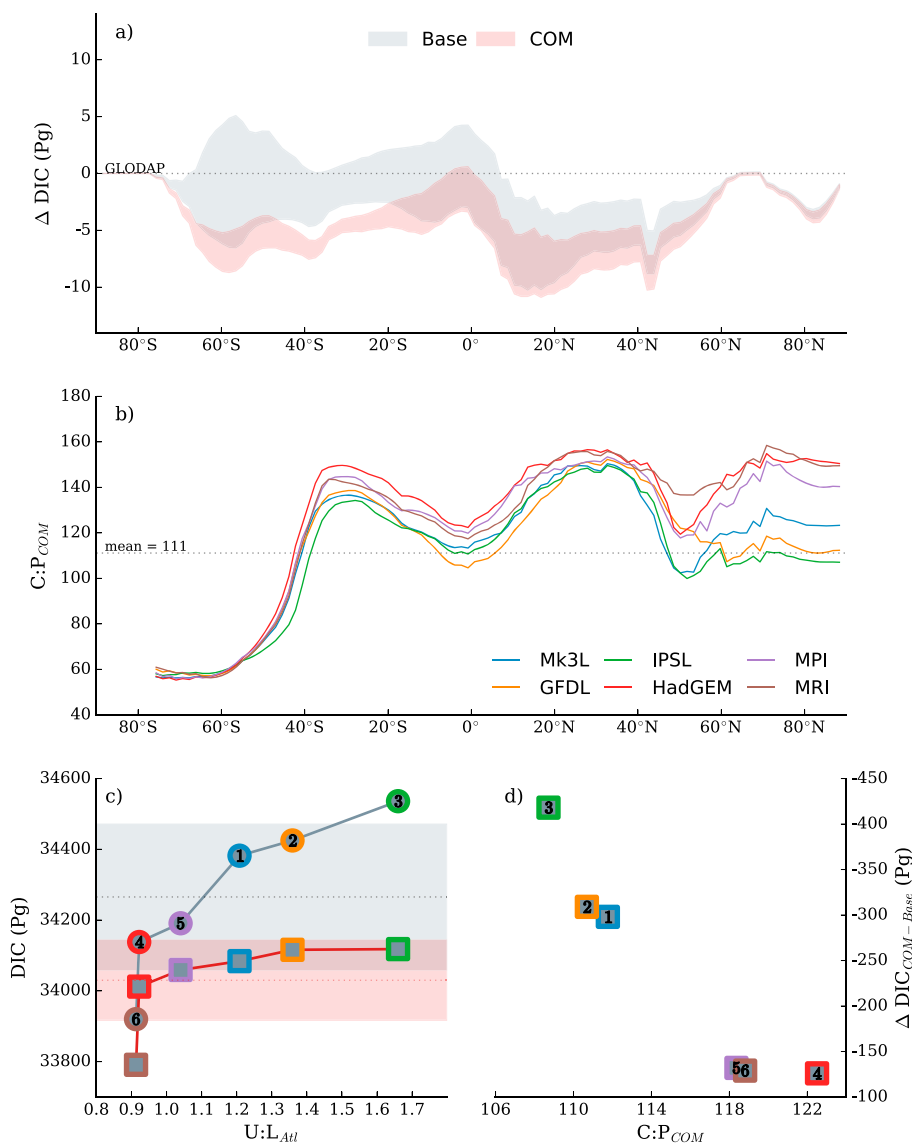


Figure 7. Changes in the total carbon content of the ocean and its major driver between the Base (grey shading) and combination (COM, pink shading) biological states. (a) The difference between the simulated and observed (Key et al., 2004) zonally integrated carbon content (Pg C) is shown for both biological states, with the shading representing one standard deviation either side of the mean across all physical states. (b) The zonally averaged C:P ratios of the COM biological state. (c) How the total carbon content of each ocean state changed between the Base (circles; grey shading) and COM (squares; pink shading). Each ocean state lost carbon under the COM biological state as material was shifted into the upper ocean and carbon was subsequently lost to the atmosphere. (d) How the magnitude of loss was mitigated by the magnitude of increase in the global mean C:P ratio, such that differences in carbon content were minimized across physical states. Physical states are Mk3L(1), GFDL(2), IPSL(3), HadGEM(4), MPI(5), and MRI(6).

Under the COM biological state, however, this relationship was eroded (Figure 8), and inter-ocean differences in NO_3 content decreased from 74 Pg N to 57 Pg N.

Greater similarity in NO_3 across physical states reflected the unique responses of nitrogen fixation and denitrification. First, all oceans lost NO_3 from the deep ocean due to low N:P ratios over the Southern Ocean (supporting information Figure S4). However, the loss of NO_3 from the deep ocean was accompanied by an increase in the upper ocean that minimized net NO_3 losses. The increase in upper ocean NO_3 was driven by increased North Atlantic nitrogen fixation and/or reduced Pacific denitrification scaled by the relative strength of the upper overturning cell (Figure 8). In GFDL, for instance, Pacific denitrification rates were heavily reduced from 85 to 25 Tg N yr⁻¹, while North Atlantic nitrogen fixation remained strong at 34 Tg N yr⁻¹.

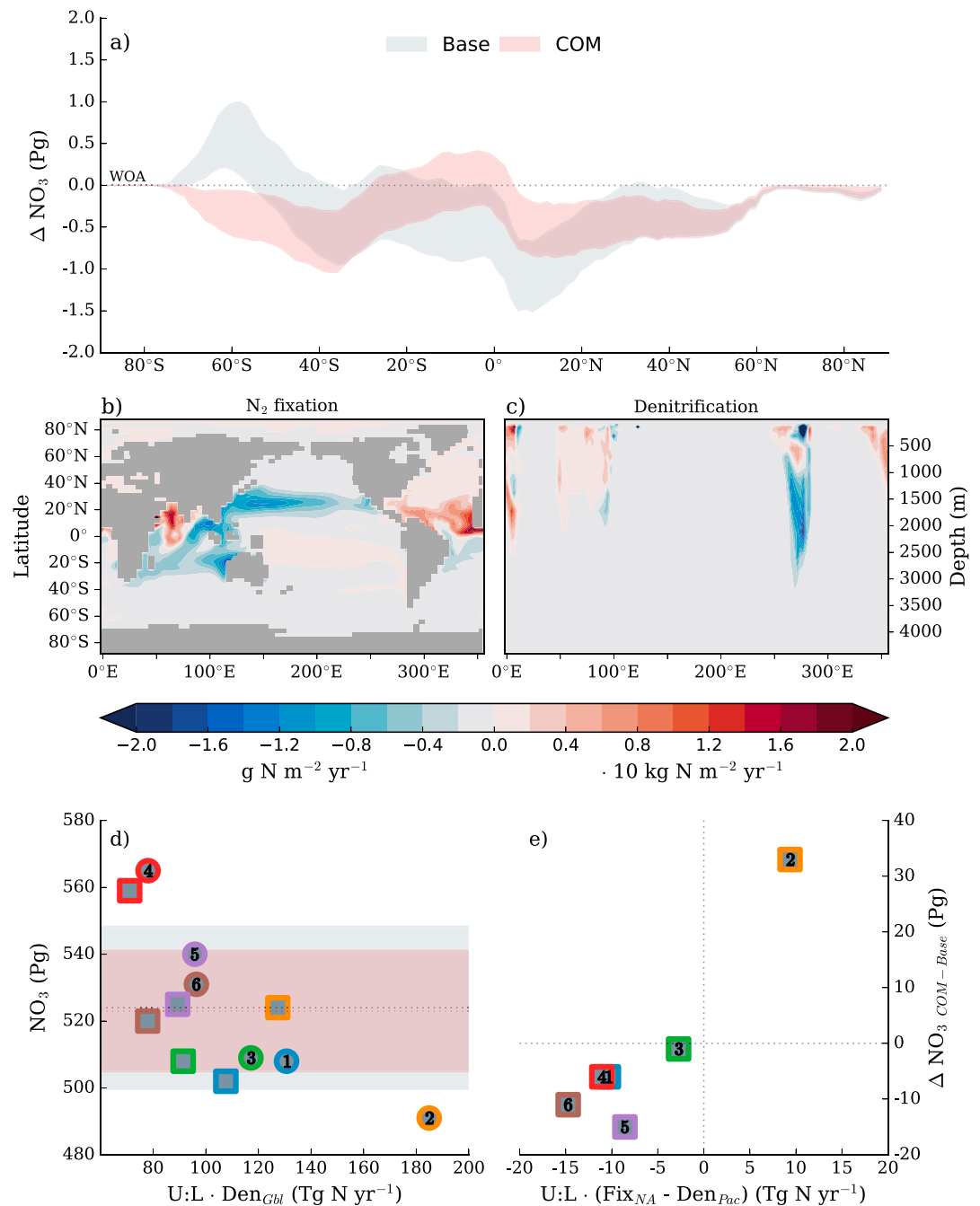


Figure 8. Changes in the total nitrogen content of the ocean and its major driver between the Base (grey shading) and combination (COM, pink shading) biological states. (a) The difference between the simulated and observed (Garcia, Locarnini, Boyer, Antonov, Baranova et al., 2013) zonally integrated nitrate content (Pg N) is shown for both biological states, with the shading representing one standard deviation either side of the mean across all physical states. (b) The depth integrated difference in nitrogen fixation ($\text{g N m}^{-2} \text{yr}^{-1}$) between the COM and Base biological states. (c) The meridional integrated difference in denitrification ($\cdot 10 \text{ kg N m}^{-2} \text{yr}^{-1}$) between the COM and Base biological states. (d) The global inventory of NO_3 could be predicted in the Base biological state (circles) by multiplying the global rate of denitrification (Den_{Gbl}) by the volumetric ratio of upper to lower overturning cells (U:L). However, this relationship was eroded in the COM biological state (squares) as changes in nitrogen fixation and denitrification reduced differences in NO_3 content across physical states. (e) The COM-Base change in NO_3 content was largely driven by the difference in North Atlantic nitrogen fixation (Fix_{NA} ; 20°N–90°N) and Pacific denitrification (Den_{Pac}) scaled by the dominance of the upper to lower overturning cells (U:L). Physical states are Mk3L(1), GFDL(2), IPSL(3), HadGEM (4), MPI(5), and MRI(6).

The fact that GFDL was dominated by a strong upper overturning cell augmented the accumulation of NO_3 in the upper Pacific under these conditions and more than offset the losses from the deep ocean caused by low Southern Ocean nitrogen export. In other oceans, a decrease in Pacific denitrification and an increase in North Atlantic nitrogen fixation was insufficient to offset the losses from the lower overturning cell. Importantly though, these regional responses in nitrogen fixation and denitrification to the physical conditions ensured that losses in global NO_3 storage were minimized.

5. Discussion

We have made three major findings in this model study. First, the marine nitrogen cycle is highly sensitive to marine biological processes and therefore provides a powerful tool for assessing the performance of biogeochemical ocean models. Second, the simulation of ocean biogeochemistry is significantly improved by allowing the marine community to respond dynamically to its environment. Third, including dynamical biological functioning reduces the sensitivity of the carbon and nitrogen cycles to changes in the ocean's physical state.

The biogeochemical parameterizations that were tested (see section 2) are simplistic when compared to the rich diversity of planktonic marine life and their complex interactions (see Worden et al., 2015, for a review). However, they expressed important features of ocean biology in an implicit way. Unproductive regions, such as the subtropical gyres, are dominated by picoplankton (Hirata et al., 2011; Kostadinov et al., 2009). These oligotrophic communities are represented in the majority by *Prochlorococcus* and *Synechococcus* and are associated with (1) high growth rates despite strongly nutrient limited conditions in the environment (Liu et al., 1997), (2) high rates of regenerated production supporting low rates of export production to the deep ocean (Henson et al., 2012; Mouw et al., 2016; Worden et al., 2004), and (3) higher stoichiometric requirements of nitrogen and carbon per unit of phosphorus (Klausmeier et al., 2004). In contrast, more productive regions are known to be dominated by large phytoplankton types, such as diatoms (Hirata et al., 2011; Kostadinov et al., 2009), and are associated with (1) relatively slower nutrient uptake rates given the nutrient-replete conditions (Gotham & Rhee, 1981a, 1981b; Smith & Yamanaka, 2007), (2) a more efficient transfer of less labile material to depth (Henson et al., 2012; Mouw et al., 2016), and (3) lower stoichiometric requirements of carbon and nitrogen per unit phosphorus (Klausmeier et al., 2004; Weber & Deutsch, 2010). In addition to these general patterns, a wide range of observed transfer efficiencies in the high latitudes (Boyd & Trull, 2007; Buesseler et al., 2007) and the efficient transfer of organics from areas overlying oxygen-poor zones (Cavan et al., 2017) were resolved. The combination of OUK (Smith et al., 2009), Rem_p (Weber et al., 2016), and V_{ele} (Galbraith & Martiny, 2015) therefore reproduced regional features of the global marine community and did so via either a direct or indirect relationship to nutrient concentrations. These patterns are consistent with an emerging understanding that variations in the biological community are important for controlling major biogeochemical cycles in the ocean (Le Quéré et al., 2005; Worden et al., 2015).

The dynamic biological functioning that was achieved by combining OUK, Rem_p , and V_{ele} within one biogeochemical model (COM) was particularly important for the marine nitrogen cycle. While other fields, like oxygen, were more sensitive to physical changes in the ocean's state, the distribution of NO_3 was the only biogeochemical field to be more strongly dependent on biological functioning than physical conditions. That marine biology is influential to the oceanic nitrogen cycle is not surprising considering that its major sources and sinks are entirely mediated by biological processes (Gruber, 2008). However, our results emphasize two useful points. First, that the distribution of NO_3 is a powerful tool for assessing biogeochemical model performance irrespective of the physical conditions. How biological processes are parameterized will alter the distribution of NO_3 more so than changing physical conditions, at least over the range associated with preindustrial climates. Second, that variable stoichiometry (V_{ele}) is key to adequately simulating the marine nitrogen cycle. Lower N:P ratios over the Southern Ocean set the deep inventory of NO_3 , while regional differences in N:P across the lower latitudes set the upper inventory by affecting regional rates of nitrogen fixation and denitrification (see section 4.5). Deviations from the Redfield ratio are thus fundamental for achieving a realistic distribution of NO_3 in the ocean, and we support the findings of Weber and Deutsch (2012) in this conclusion. Considering these two points, we suggest that assessment protocols for ocean biogeochemical models (e.g., Orr et al., 2017) formally include the marine nitrogen cycle, in addition to preformed and regenerated PO_4 (Duteil et al., 2012), as a useful performance indicator for biological processes.

With that being said, our simulations excluded some key processes that may have contributed to the original bias in the Base biogeochemical fields. The major biogeochemical process that was excluded was sedimentary denitrification. Sedimentary denitrification is the largest contributor to the global rate of fixed nitrogen loss and is estimated to be roughly 1.8-fold that of pelagic denitrification (Eugster & Gruber, 2012). Applying this ratio to the denitrification rates of the Base biological state gives sedimentary and pelagic denitrification rates of 64–108 Tg N yr⁻¹ and 35–60 Tg N yr⁻¹, respectively, which bare striking resemblance to the observation-constrained estimates of Eugster and Gruber (2012). Spreading NO₃ losses across a greater spatial extent via sedimentary denitrification may therefore have reconciled the overestimation of NO₃ in the deep ocean. However, the bulk of sedimentary NO₃ loss is known to occur primarily in water depths less than 1,000 m (Gruber & Sarmiento, 1997). Due to the coarse resolution of our OGCM and its overestimation of anoxic water, much pelagic denitrification already occurred at depths where sedimentary denitrification is known to occur. While we cannot unequivocally say that the inclusion of sedimentary denitrification would not be beneficial, we argue that its inclusion would only marginally rectify the deep upper ocean NO₃ bias.

Important physical processes were also not accounted for in the simulations due to the coarse resolution of the ocean model. Mesoscale and submesoscale motions, such as eddy-induced stirring and turbulence, are important to reproduce a credible large-scale circulation. The 2.8° in longitude by 1.6° in latitude grid spacing of the OGCM is larger than any resolution required to adequately resolve these dynamics (Hallberg, 2013). The inconsistencies between simulated and observed overturnings of intermediate waters in the North Pacific and Southern Ocean are testament to this fact. All ocean states, except the Mk3L, produced net upwelling of intermediate waters in the Southern Ocean in contrast with estimates (Iudicone et al., 2011). Intermediate waters are a major supply of nutrients to the mesopelagic ocean (Sarmiento et al., 2004), and the inability of each physical state to generate realistic subduction rates likely contributed to the vertical bias in nutrients that was common across all states. The overturning circulations were also biased by an unrealistic formation of Southern Ocean dense waters via convective mixing in the open ocean, rather than on the Antarctic shelves (Heuzé et al., 2013). The multiple circulations shared the same model physics and architecture, and it is therefore unsurprising that all circulations featured the same biases, albeit to a greater or lesser extent.

Nonetheless, the inclusion of dynamic biological functioning improved the distribution of NO₃ markedly. It also altered the response of the NO₃ reservoir to physical change, dampening its sensitivity. Under the Base biological state, the oceanic inventory of NO₃ could be predicted by taking the product of the circulation type, U:L (see section 4.1), and the global denitrification rate, Den_{GBI} (see section 4.5). However, this simple relationship was eroded under the COM biological state as the NO₃ inventory became more dependent on how biology responded to its environment. The NO₃ content of the deep ocean was set by the N:P ratio over the Southern Ocean. Variable stoichiometry (V_{ele}) allowed those oceans dominated by a more voluminous and nutrient-rich lower cell to develop lower N:P ratios, and these states lost more NO₃. In contrast, the NO₃ content of the upper ocean was set by basin-specific rates of nitrogen fixation and denitrification. Stratified oceans with weaker nutrient delivery (U:L_{Atl} ≤ 1) experienced stronger increases in nitrogen fixation, particularly in the North Atlantic, as higher N:P ratios increased the competitive advantage of nitrogen fixers (Landolfi et al., 2015). Meanwhile, oceans with stronger nutrient delivery experienced reduced denitrification, particularly in the Pacific, as N_{den}:P values were lowered. These biological responses to physical conditions increased North Atlantic sources from 14–66 to 29–64 Tg N yr⁻¹ and decreased Pacific sinks from 67–32 to 25–20 Tg N yr⁻¹ between the Base and COM experiments. The role of the North Atlantic as a *factory of fixed nitrogen*, which exports the majority of its newly fixed nitrogen into NADW (McGillicuddy, 2014), and the role of the Pacific as a *leaking storage warehouse* were therefore made more similar across different physical states. We have some confidence that these changes are reasonable reflections of reality because they were associated with a significant improvement in the simulated NO₃ field, although rates of nitrogen fixation for the Pacific were too low compared to observations (Luo et al., 2012). However, the relative rate of sources and sinks and their locations within each basin are important for the NO₃ inventory. In addition to the necessity of non-Redfield ratios (Weber & Deutsch, 2012), we therefore also support the conclusions of Weber and Deutsch (2014) in that basin-specific rates of nitrogen fixation and denitrification are important for setting the oceanic inventory of fixed nitrogen. But we extend and combine these theories in the context of dynamic biological functioning under different circulation states, where dynamic biological functioning under different physical conditions helps to stabilize the NO₃ content of the ocean.

The greater resilience to physical changes was also observed in the marine carbon cycle, which showed a ~50% reduction in the range of carbon inventories across the six physical states from 616 to 327 Pg C.

If MRI was excluded, which suffered excessive ventilation of the North Pacific, differences between states were less than 100 Pg C. Smaller differences between oceans under the COM biological state was caused by the dynamic response of biology to nutrient delivery, which reduced differences in export production by 0.4 Pg C yr^{-1} . Under the nondynamic biological state, the total carbon content of the ocean was strongly dependent on the strength of the AMOC ($U:L_{\text{Atl}}$), which fueled greater export production through stronger upwelling of nutrients. Previous studies have also shown this relationship (Mariotti et al., 2012; Schmittner, 2005), whereby variations in the AMOC are directly proportional to global rates of export production. The introduction of dynamic biological functioning allowed nutrient-limited oceans with a weak AMOC ($U:L_{\text{Atl}} \leq 1$) to respond by increasing the efficiency of nutrient uptake (OUK), C:P stoichiometry (V_{ele}), and transfer efficiency (Rem_p), all in accordance with observed regional features of marine communities (see above). The strong relationship between circulation, export production, and carbon storage was therefore diminished but not altogether removed. Oceans with a strong AMOC were still associated with greater export production and carbon inventories (Mariotti et al., 2012; Schmittner, 2005), and oceans that ventilated the North Pacific were associated with a loss of carbon to the atmosphere (Galbraith et al., 2007). Biological functioning simply responded in such a way as to mitigate the effect of circulation differences. An independent study by Tanioka and Matsumoto (2017) has demonstrated similar results by including variations in C:P. The potential for a responsive biology to minimize the effect of physical change on carbon export is therefore only recently realized. We extend the findings of Tanioka and Matsumoto (2017) to include variations in production, remineralization, and a wider stoichiometry ($\text{C:N:P:O}_{\text{rem}}:\text{N}_{\text{den}}$) and show that accounting for these variations has significant consequences for carbon storage over millennial time scales.

6. Conclusions

Altogether, these results make a strong case for the inclusion of dynamic biological functioning within biogeochemical ocean models that seek to determine climate-driven changes in carbon and other properties. Our understanding of the climate system, and by extension our ability to make accurate predictions of its behavior, relies on studies that simulate the exchange of greenhouse gases between the major reservoirs (Falkowski et al., 2000). Ocean biogeochemical models are essential to these studies and have demonstrated the importance of the ocean and its biological pump for setting atmospheric CO_2 concentrations (Buchanan et al., 2016; Menviel et al., 2012; Schmittner & Somes, 2016). But it is important to recognize that the insights garnered from these and other studies have involved rudimentary representations of what is a complex biological community (Worden et al., 2015).

The challenge, therefore, is to include the wider effects of important biogeochemical processes using interpretable formulations. In this study, we find that the inclusion of some simple parameterizations that introduce dynamic responses in production (Smith et al., 2009), remineralization (Weber et al., 2016), and stoichiometry (Galbraith & Martiny, 2015) can yield large-scale features of the ocean's biological pump that are representative of reality. By implementing these dynamic parameterizations, we make three major findings.

1. The marine nitrogen cycle is highly sensitive to how the biological pump is represented and fundamentally requires variations in organic matter stoichiometry. We therefore suggest that assessment protocols for ocean biogeochemical models formally include the marine nitrogen cycle to constrain biological processes.
2. A dynamic biological functioning is important for more accurately simulating ocean biogeochemistry.
3. A dynamic biological functioning has considerable potential to stabilize globally important properties, such as carbon, under physical change.

7. Data Availability

Model output for this work is held by the Australian National Computational Infrastructure data portal and is available for download at <https://doi.org/10.4225/41/5a1b6aa448c32>.

Appendix A: Base Ocean Biogeochemistry in CSIRO Mk3L

The biogeochemical model is nested within the OGCM of the CSIRO Mk3L climate system model (Phipps et al., 2011, 2012). The OGCM has a horizontal resolution of $2.8^\circ \times 1.6^\circ$ in the longitudinal and latitudinal dimensions,

respectively, and 21 uneven vertical levels. The vertical resolution of the OGCM is highest at the surface and coarsest at depth, with the upper level covering the first 25 m and the final depth covering 450 m.

Organic matter in the ocean model is produced by three types of phytoplankton: a general type, diazotrophs, and calcifiers. The following equations describe how organic matter of the general phytoplankton group is simulated. A full description of diazotrophic production as part of the equations governing the marine nitrogen cycle is described in Appendix C. Calcifiers represent a constant 8% of the general phytoplankton group, a large fraction of that produced at the surface (F_z^{PIC}) transferred to deep waters according to the exponential function $F_z^{\text{PIC}} = e^{(\frac{z}{3500})}$, and they consume DIC and ALK at a ratio of 1:1 and 2:1 of the general phytoplankton group (Matear & Lenton, 2014).

The ocean biogeochemical model simulates organic matter cycling in the general phytoplankton type via the three major components: production at the surface, remineralization, and the quantities of tracers that are involved in these exchanges.

A1. Organic Matter Production

First, the maximum daily growth rate (μ) is calculated using sea surface temperature (Eppley, 1972). This relationship defines how primary producers grow under optimal conditions (i.e., where nutrients and light are not limiting).

$$\mu = 0.59 \cdot 1.0635^T \quad (\text{A1})$$

Second, the availability of light and nutrients is applied to reduce the growth rate to simulate the effect of suboptimal conditions. If the concentration of nutrients or light are limiting, then the maximum growth rate set by temperature cannot be achieved. In CSIRO Mk3L, nutrient limitation terms for PO_4 , NO_3 , and Fe are calculated using the hyperbolic equations governing enzyme reactions, otherwise known as Michaelis-Menten kinetics (Dugdale, 1967), where

$$\text{PO}_{4\text{lim}} = \frac{\text{PO}_4}{\text{PO}_4 + K_{\text{PO}_4}} \quad (\text{A2})$$

$$\text{NO}_{3\text{lim}} = \frac{\text{NO}_3}{\text{NO}_3 + K_{\text{NO}_3}} \quad (\text{A3})$$

$$\text{Fe}_{\text{lim}} = \frac{\text{Fe}}{\text{Fe} + K_{\text{Fe}}} \quad (\text{A4})$$

In the above, the limitation term for each nutrient varies between 0 and 1, and the point at which the limitation term is equal to 0.5 is equal to the value set by the half-saturation coefficient (K_{nutrient}).

Half-saturation coefficients for each nutrient have been experimentally derived for many phytoplankton taxa, which show large interspecies differences (e.g., Timmermans et al., 2004). For simplicity, though, these are set at constant values of 0.05 mmol $\text{PO}_4 \text{ m}^{-3}$ (Smith, 1982), 0.75 mmol $\text{NO}_3 \text{ m}^{-3}$ (Carpenter & Guillard, 1971; Eppley et al., 1969), and 0.1 $\mu\text{mol Fe m}^{-3}$ (Timmermans et al., 2001). With the exception of PO_4 , which was tuned upward, these values coincide with the lower range of estimates made by each of these studies so that smaller, open ocean phytoplankton are represented over larger, predominantly coastal taxa. The most limiting factor of these nutrient limitation terms, as well as the light limitation term ($F(I)$) described in Appendix A of Matear and Lenton (2014), is then applied against the maximum daily growth rate (μ) to find net primary production. Finally, a scaling parameter (S_{NPP}) equals to 0.005 mmol P m^{-3} is applied to convert to export production in units of mmol P m^{-3} . The final equation governing export production is therefore

$$\text{Particulate Organic Matter} = S_{\text{NPP}} \cdot \mu(T) \cdot \min(\text{PO}_{4\text{lim}}, \text{NO}_{3\text{lim}}, \text{Fe}_{\text{lim}}, F(I)) \quad (\text{A5})$$

A2. Remineralization of Organic Matter

The transfer of organic matter to the ocean interior is controlled by a Martin curve (Martin et al., 1987), where the amount of particulate organic matter at a given depth (F_z^{POC}) is calculated as a function of the concentration of particulate organic matter at 100 m depth (F_{100}^{POC}) and depth itself (z).

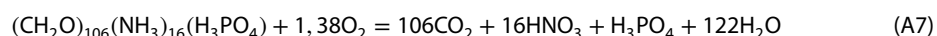
$$F_z^{\text{POC}} = F_{100}^{\text{POC}} \cdot \left(\frac{z}{100}\right)^b \quad (\text{A6})$$

Martin et al. (1987) applied this function to oligotrophic stations in the northeast Pacific and found optimal fits to organic fluxes using a b exponent of -0.858 . The biogeochemical model sets the b exponent to -0.858 . If organic matter is still present in the last depth level, then all organic matter is remineralized to ensure mass balance.

A3. Elemental Ratios

The quantity of tracers involved in organic matter cycling is prescribed according to the Redfield ratio. By analyzing the elemental components of organic matter, Redfield et al. (1937) and Fleming (1940) identified that carbon, nitrogen, and phosphorus varied proportionally in a ratio of 106:16:1.

Redfield (1963) then applied these ratios to calculate the oxygen produced and consumed during the production and remineralization of organic matter, respectively, and obtained a C:N:P:O₂ ratio of 106:16:1:–138. These ratios assume that the composition and remineralization of marine organic matter can be defined by the following stoichiometric formula.



The ratio of Redfield (1963) therefore makes an implicit assumption regarding the quantities of hydrogen and oxygen atoms that accompany the carbon, nitrogen, and phosphorus to compose marine organic matter (Anderson, 1995).

$$\text{H:P} = 2\text{C:P} + 3\text{N:P} + 3 = 263 \quad (\text{A8})$$

$$\text{O:P} = \text{C:P} + 4 = 110 \quad (\text{A9})$$

Once a C:N:P:H:O ratio is known, we calculate the amount of dissolved oxygen (O₂) needed to completely remineralize the organic matter into its major inorganic constituents (CO₂, NO₃, and PO₄) using the following formula (Anderson, 1995; Paulmier et al., 2009):

$$\text{O}_2:\text{P} = -(\text{C:P} + 0.25\text{H:P} - 0.5\text{O:P} - 0.75\text{N:P} + 1.25) - 2\text{N:P} = -138 \quad (\text{A10})$$

And we find the original ratio given by Redfield (1963). Likewise, the consumption of nitrate due to complete denitrification (suboxic remineralization) can also be calculated according to the formula of Paulmier et al. (2009):

$$\text{NO}_3:\text{P} = -(0.8\text{C:P} + 0.25\text{H:P} - 0.5\text{O:P} - 0.75\text{N:P} + 1.25) + 0.6\text{N:P} = -94.4 \quad (\text{A11})$$

Thus, the exchange of elements through the biological pump is prescribed according to a C:N:P:O₂:NO₃ ratio of 106:16:1:–138:–94.4.

Appendix B: Formation Rates of Southern Source Intermediate Waters

The formation rates of AAIW and SAMW were found via a three step process requiring salinity (practical salinity unit), density (kg m⁻³), mixed-layer depth (m), and the horizontal and vertical transports of water (m⁻³ s⁻¹) through the faces of each grid cell.

1. Using the annual and zonal average of salinity, we found the salinity minimum at 30°S for all six physical states. A defining feature of AAIW is the prominent salinity minimum tongue. The isopycnals corresponding to AAIW were then found by taking the “full width at half maximum” around the salinity minimum of the depth profile (Figure B1), using the deep salinity at 2,200 m as the reference point. Finally, the isopycnals for SAMW were included by adding 0.5 kg m⁻³ of the lighter isopycnals above AAIW. The inclusion of SAMW using isopycnals 0.5 kg m⁻³ lighter than AAIW was informed by the multiple modes of SAMW that exist at densities between 1026.7 and 1027.3 kg m⁻³ circumpolarly (Herraiz-Borreguero & Rintoul, 2011). Isopycnals for AAIW and SAMW were combined to represent Southern Source Intermediate Water (SSIW).
2. The horizontal and vertical transports (m³ s⁻¹) we calculated using velocities (m s⁻¹) and the area of grid cell faces. Transports were only considered at those grid points where isopycnals belonging to SSIW outcropped. Because most isopycnals did not outcrop at the surface, outcropping at depth was included by finding those grid points where the depth of annual maximum mixed layers intersected with the isopycnals. The locations of grid cells and their transports where isopycnals outcropped were saved.

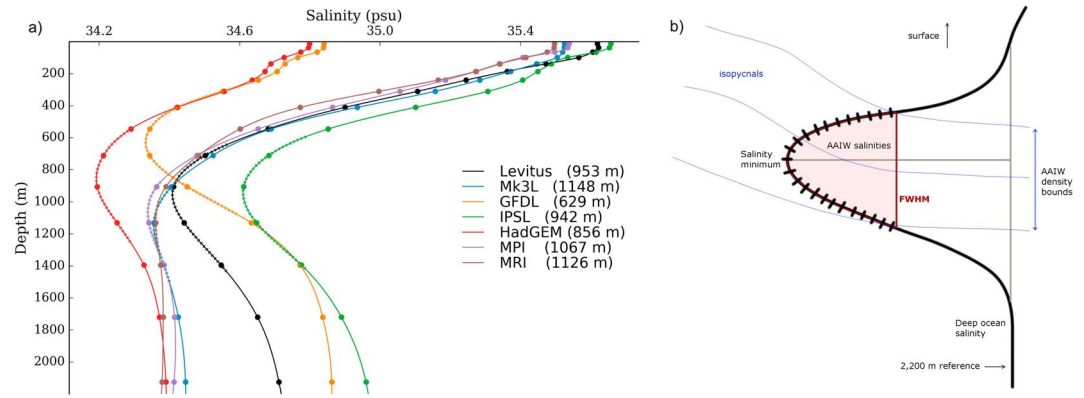


Figure B1. A graphical depiction of determining the isopycnals corresponding to Antarctic Intermediate Water (AAIW) for all physical states. (a) Annual and zonal mean salinity profiles for observations and the six physical states at 30°S. The stippled area represents the full width at half maximum (FWHM) around the salinity minimum. (b) A schematic description of what the full width at half maximum (FWHM) represents with respect to the salinity minimum of AAIW, and the isopycnals (blue) that are associated with it. The pink shaded area represents the selected salinities and isopycnals of the FWHM.

3. Transports across the annual maximum mixed layer (H) into isopycnal surfaces at all valid grid cells (i,j,k) were calculated as

$$SSIW_{i,j,k} = -\left(U_H \cdot \frac{\partial h}{\partial x} + V_H \cdot \frac{\partial h}{\partial y} \right) - W_H \quad (B1)$$

A positive horizontal (eastward or northward) transport therefore only contributed to SSIW subduction if the change in mixed-layer depth was negative in that dimension (i.e., shoaling). Likewise, a positive transport contributed to SSIW upwelling if the mixed-layer depth deepened. These positive and negative transports through the isopycnal surfaces of SSIW were summed in the Southern Hemisphere to give total subduction and upwelling rates, respectively (see Table 2).

Appendix C: The Marine Nitrogen Cycle in CSIRO Mk3L

C1. Sources

The marine nitrogen cycle is unique in that its sources and sinks are almost entirely mediated by biology (Gruber, 2008). Where other elemental cycles, such as carbon and oxygen, have a significant air-sea gas exchange component, the source of biologically available nitrogen to the ocean is mostly due to nitrogen fixation (Brandes et al., 2007). Specialized photosynthetic organisms, called nitrogen fixers, are able to utilize dinitrogen gas (N₂), which is abundant throughout the ocean. By breaking the strong triple bond of N₂ to create organic matter, nitrogen fixers convert an inert form of nitrogen into biologically available forms. The organic matter created through nitrogen fixation is then remineralized in the ocean interior to release fixed nitrogen, providing a constant source of NO₃ to the ocean interior.

In CSIRO Mk3L, the production of organic matter via nitrogen fixation (POM_{fix}) is explicitly calculated as a function of temperature (T), nitrate (NO₃), and iron (Fe), with an additional sea ice component, according to the following equations:

$$POM_{fix} = S_{NPP_{fix}} \cdot \mu_{fix}(T) \cdot Lim_{fix}(NO_3, Fe) \cdot (1 - I_{co}) \quad (C1)$$

where

$$S_{NPP_{fix}} = 0.005 \text{ mmol PO}_4 \text{ m}^{-3} \quad (C2)$$

$$\mu_{fix} = \max(0.005, -0.0042T^2 + 0.2253T - 2.7819) \quad (C3)$$

$$Lim_{fix} = \min(e^{-NO_3}, \max(0.0, \tanh(2Fe - 0.6))) \quad (C4)$$

In the above, S_{NPP_{fix}} represents a scaling parameter in mmol PO₄ m⁻³ to represent the conversion of total organic matter into that which is exported from the surface ocean. Its value was tuned to produce global

additions of NO_3 via nitrogen fixation within the estimates of previous authors (Brandes et al., 2007; Codispoti, 2007). μ_{fix} is the maximum growth rate per day of nitrogen fixers and is a function of sea surface temperature ($^{\circ}\text{C}$). The relationship between μ_{fix} and T is quadratic and taken from Kriest and Oschlies (2015), where growth only occurs between ~ 18 and 34°C and hits a maximum rate of 0.2395 d^{-1} at $T = 26.82^{\circ}\text{C}$. However, based on recent observations that show the presence of nitrogen fixation in cooler environments (Blais et al., 2012; Shiozaki et al., 2015), a positive minimum rate of 0.005 d^{-1} is set globally.

Lim_{fix} contains the nutrient limitations on nitrogen fixation. The first term of Lim_{fix} represents the requirement that NO_3 be limiting in the environment. As NO_3 concentrations exceed 3.0 mmol m^{-3} , the production of POM_{fix} continues to decline asymptotically beneath 5% of its maximum potential μ_{fix} . This parameterization is informed by the inhibition of nitrogen fixation at NO_3 concentrations above 5 mmol m^{-3} (Holl & Montoya, 2005). The second term represents the high requirement of nitrogen fixers for Fe, where no nitrogen fixation can occur when iron concentrations fall below $0.3 \mu\text{mol m}^{-3}$. This lower bound is somewhat arbitrary but is informed by observations of nitrogen fixation only occurring above a background rate when iron concentrations exceeded $0.2\text{--}0.4 \mu\text{mol m}^{-3}$ in the Atlantic (Moore et al., 2009). As Fe concentrations exceed $0.3 \mu\text{mol m}^{-3}$ the limitation by iron is quickly reduced, so that Fe limitation becomes negligible at concentrations greater than $1 \mu\text{mol m}^{-3}$. Finally, the term I_{co} represents the concentration of sea ice, so that, where sea ice coverage is 100%, no nitrogen fixation can occur. Light was ignored as a limiting factor because of its strong correlation with temperature (Luo et al., 2014), and considering recent work by McGillicuddy (2014) showing that light has no limiting effect to nitrogen fixation in the Atlantic.

The production of organic matter by nitrogen fixers (POM_{fix}) is made separate from the production of organic matter by other phytoplankton (POM). This distinction was not only necessary to prescribe different environmental limitations but also allowed a unique stoichiometry to be prescribed. A $\text{PO}_4:\text{NO}_3:\text{DIC}$ stoichiometry for POM_{fix} was set to 1:50:331, in line with the studies of Karl and Letelier (2008) and Mills and Arrigo (2010). Although nitrogen fixation is not limited by phosphate in CSIRO Mk3L, the production of POM_{fix} does involve the uptake of PO_4 from the surface ocean. PO_4 may therefore be removed past zero if nitrogen fixation is strong enough. Excluding PO_4 as a limiting nutrient to nitrogen fixers was informed by the primary importance of NO_3 and Fe (Weber & Deutsch, 2014), the ability of nitrogen fixers to access dissolved organic phosphorus in the water column (Dyhrman et al., 2006; Landolfi et al., 2015; Moore et al., 2009), which is not accounted for in our model. Consequently, excluding PO_4 allowed the model to best reproduce known patterns of nitrogen fixation in the oceans (Westberry & Siegel, 2006) and match other well performing models (Landolfi et al., 2015; McGillicuddy, 2014).

The addition of NO_3 due to nitrogen fixation was complemented with the deposition of reactive nitrogen to the surface of the ocean from the atmosphere. The monthly climatology of the combined wet and dry deposition of reactive nitrogen to the surface layer was calculated from the final 30 years of output produced by the Goddard Institute for Space Studies model during its preindustrial experiment as part of the CMIP5 model contingent. The initial fields that the Goddard Institute for Space Studies model used were produced by Lamarque et al. (2013). The annual total deposition of nitrogen to the surface ocean using this climatology is $\sim 13 \text{ Tg N yr}^{-3}$.

C2. Sinks

Denitrification involves the reverse of nitrogen fixation in simplistic terms, whereby the consumption of NO_3 at depth produces N_2 and therefore removes biologically available nitrogen from the ocean. This process occurs in the ocean interior where oxygen concentrations are low. NO_3 therefore represents an alternative to O_2 during remineralization. The computation of denitrification in CSIRO Mk3L is a function of O_2 , NO_3 , and the concentration of POM and POM_{fix} that enters a given depth level. First, the relationship between O_2 and the strength of denitrification (r_{den}) is set according to a sigmoidal function:

$$r_{\text{den}} = \frac{1}{1 - e^{0.5x} + e^{\text{O}_2 - 0.5x}} \quad (\text{C5})$$

In the above, r_{den} is made to vary between 0 and 1 depending on the O_2 concentration, for which an upper limit at which denitrification ceases is set by $x \text{ mmol O}_2 \text{ m}^{-3}$. At concentrations of O_2 above x only oxalic remineralization can take place. The O_2 concentration at which denitrification starts to occur is set at 7.5 mmol m^{-3} . This parameterization ensures that 50% of organic matter is remineralized by denitrification at an oxygen

concentration of 3.75 mmol m^{-3} , and that $> 97\%$ of organic matter is remineralized by NO_3 at O_2 concentrations less than 1 mmol m^{-3} .

Second, the strength of denitrification (r_{den}) is reduced if the concentration of NO_3 is deemed to be limiting. If no NO_3 is present, then denitrification will not occur. Likewise, if the removal of NO_3 due to denitrification exceeds the concentration of NO_3 that is available, then r_{den} will be reduced so that NO_3 is not removed past zero. However, with only this limitation in place the concentrations of NO_3 were completely depleted in the OMZs. This has been observed in other biogeochemical models (Moore & Doney, 2007; Schmittner et al., 2008) and occurs as high rates of nitrogen fixation above the zone of denitrification cause a positive feedback of oxygen depletion and NO_3 removal. Importantly though, it is not an accurate reflection of the true concentrations of NO_3 in the OMZs, which are observed to be ~ 15 to 40 mmol m^{-3} (Codispoti & Richards, 1976; Voss et al., 2001). Therefore, an additional constraint ($\text{relax}_{\text{den}}$) was placed on r_{den} to artificially simulate slower rates of denitrification relative to oxic remineralization (Su et al., 2015).

$$\text{relax}_{\text{den}} = \max \left(0.0, -1 + 2 \cdot \frac{\text{NO}_3}{40} \right) \quad (\text{C6})$$

$$\text{if } \text{relax}_{\text{den}} < r_{\text{den}}, \text{ then } r_{\text{den}} = \text{relax}_{\text{den}} \quad (\text{C7})$$

This addition ensured that denitrification could not occur at concentrations of NO_3 less than 20 mmol m^{-3} , and that NO_3 concentrations within denitrifying zones always remained above the lower bounds of observations ($\sim 15 \text{ mmol m}^{-3}$).

As a final consideration, the addition of nitrogen fixation and denitrification to CSIRO Mk3L required an alteration to the calculation of alkalinity. The addition of NO_3 molecules via nitrogen fixation and atmospheric deposition was accompanied by an addition of approximately equal amounts of protons to the water column (Wolf-Gladrow et al., 2007) and requires a reduction in alkalinity. Meanwhile, the removal of NO_3 molecules via denitrification requires an addition of alkalinity. The sources and sinks of alkalinity therefore partly mirror the sources and sinks of NO_3 .

Acknowledgments

We wish to thank the Australian Research Council's Centre of Excellence for Climate System Science and the Tasmanian Partnership for Advanced Computing (TPAC) for facilitating the research. This research was supported under the Australian Research Council's Special Research Initiative for the Antarctic Gateway Partnership (Project ID SR140300001). The authors wish to acknowledge the use of the Ferret program for the analysis undertaken in this work. Ferret is a product of NOAA's Pacific Marine Environmental Laboratory (Information is available at <http://ferret.pmel.noaa.gov/Ferret/>). The matplotlib package (Hunter, 2007), Iris and Cartopy packages (<http://scitools.org.uk/>), and the cmocean package (Thyng et al., 2016) were all used for producing the figures. We acknowledge the World Climate Research Programme's Working Group on Coupled Modelling, which is responsible for CMIP, and we thank the climate modeling groups (listed in Table 1 of this paper) for producing and making available their model output. For CMIP the U.S. Department of Energy's Program for Climate Model Diagnosis and Intercomparison provides coordinating support and led development of software infrastructure in partnership with the Global Organization for Earth System Science Portals. Finally, we would like to thank Tim DeVries, Stephanie Downes, and the biogeochemistry discussion group at the Institute of Marine and Antarctic Studies for providing feedback and advice.

References

- Anderson, L. A. (1995). On the hydrogen and oxygen content of marine phytoplankton. *Deep Sea Research Part I: Oceanographic Research Papers*, 42(9), 1675–1680. [https://doi.org/10.1016/0967-0637\(95\)00072-E](https://doi.org/10.1016/0967-0637(95)00072-E)
- Anderson, L. A., & Sarmiento, J. L. (1994). Redfield ratios of remineralization determined by nutrient data analysis. *Global Biogeochemical Cycles*, 8(1), 65–80. <https://doi.org/10.1029/93GB03318>
- Aumont, O., van Hulten, M., Roy-Barman, M., Dutay, J.-C., Éthé, C., & Gehlen, M. (2017). Variable reactivity of particulate organic matter in a global ocean biogeochemical model. *Biogeosciences*, 14(9), 2321–2341. <https://doi.org/10.5194/bg-14-2321-2017>
- Behrenfeld, M. J., & Falkowski, P. G. (1997). Photosynthetic rates derived from satellite-based chlorophyll concentration. *Limnology and Oceanography*, 42(1), 1–20. <https://doi.org/10.4319/lo.1997.42.1.0001>
- Bendtsen, J., Hilligsøe, K. M., Hansen, J. L. S., & Richardson, K. (2015). Analysis of remineralisation, lability, temperature sensitivity and structural composition of organic matter from the upper ocean. *Progress in Oceanography*, 130, 125–145. <https://doi.org/10.1016/j.pocean.2014.10.009>
- Berelson, W. (2001). The flux of particulate organic carbon into the ocean interior: A comparison of four U.S. JGOFS regional studies. *Oceanography*, 14(4), 59–67. <https://doi.org/10.5670/oceanog.2001.07>
- Blais, M., Tremblay, J. É., Jungblut, A. D., Gagnon, J., Martin, J., Thaler, M., et al. (2012). Nitrogen fixation and identification of potential diazotrophs in the Canadian Arctic. *Global Biogeochemical Cycles*, 26, GB3022. <https://doi.org/10.1029/2011GB004096>
- Bond, G., Showers, W., Cheseby, M., Lotti, R., Almasi, P., DeMenocal, P., et al. (1997). A pervasive millennial-scale cycle in North Atlantic Holocene and glacial climates. *Science*, 278(5341), 1257–1266. <https://doi.org/10.1126/science.278.5341.1257>
- Boulaudid, M., & Minster, J. F. (1989). Oxygen consumption and nutrient regeneration ratios along isopycnal horizons in the Pacific Ocean. *Marine Chemistry*, 26(2), 133–153. [https://doi.org/10.1016/0304-4203\(89\)90057-1](https://doi.org/10.1016/0304-4203(89)90057-1)
- Boyd, P., & Trull, T. (2007). Understanding the export of biogenic particles in oceanic waters: Is there consensus? *Progress in Oceanography*, 72(4), 276–312. <https://doi.org/10.1016/j.pocean.2006.10.007>
- Boyd, P. W., & Doney, S. C. (2002). Modelling regional responses by marine pelagic ecosystems to global climate change. *Geophysical Research Letters*, 29(16), 1806. <https://doi.org/10.1029/2001GL014130>
- Brandes, J. a., Devol, A. H., & Deutsch, C. (2007). New developments in the marine nitrogen cycle. *Chemical Reviews*, 107(2), 577–589. <https://doi.org/10.1021/cr050377t>
- Buchanan, P. J., Matear, R. J., Lenton, A., Phipps, S. J., Chase, Z., & Etheridge, D. M. (2016). The simulated climate of the Last Glacial Maximum and insights into the global marine carbon cycle. *Climate of the Past*, 12(12), 2271–2295. <https://doi.org/10.5194/cp-12-2271-2016>
- Buesseler, K. O., Lamborg, C. H., Boyd, P. W., Lam, P. J., Trull, T. W., Bidigare, R. R., et al. (2007). Revisiting carbon flux through the ocean's twilight zone. *Science*, 316, 567–570. <https://doi.org/10.1126/science.1137959>
- Carpenter, E. J., & Guillard, R. R. L. (1971). Intraspecific differences in nitrate half-saturation constants for three species of marine phytoplankton. *Ecology*, 52(1), 183–185.
- Cavan, E. L., Trimmer, M., Shelley, F., & Sanders, R. (2017). Remineralization of particulate organic carbon in an ocean oxygen minimum zone. *Nature Communications*, 8(14), 847. <https://doi.org/10.1038/ncomms14847>

- Cocco, V., Joos, F., Steinacher, M., Frölicher, T. L., Bopp, L., Dunne, J., et al. (2013). Oxygen and indicators of stress for marine life in multi-model global warming projections. *Biogeosciences*, 10(3), 1849–1868. <https://doi.org/10.5194/bg-10-1849-2013>
- Codispoti, L. (2007). An oceanic fixed nitrogen sink exceeding 400 Tg N a⁻¹ vs the concept of homeostasis in the fixed-nitrogen inventory. *Biogeosciences*, 4(2), 233–253. <https://doi.org/10.5194/bg-4-233-2007>
- Codispoti, L. A., & Richards, F. A. (1976). An analysis of the horizontal regime of denitrification in the eastern tropical North Pacific. *Limnology and Oceanography*, 21(3), 379–388. <https://doi.org/10.4319/lo.1976.21.3.0379>
- de Boyer Montégut, C., Madec, G., Fischer, A. S., Lazar, A., & Iudicone, D. (2004). Mixed layer depth over the global ocean: An examination of profile data and a profile-based climatology. *Journal of Geophysical Research*, 109, C12003. <https://doi.org/10.1029/2004JC002378>
- Deppeler, S. L., & Davidson, A. T. (2017). Southern ocean phytoplankton in a changing climate. *Frontiers in Marine Science*, 4, 40. <https://doi.org/10.3389/fmars.2017.00040>
- Ducklow, H. W., Wilson, S. E., Post, A. F., Stammerjohn, S. E., Erickson, M., Lee, S., et al. (2015). Particle flux on the continental shelf in the Amundsen Sea Polynya and Western Antarctic Peninsula. *Elementa: Science of the Anthropocene*, 3, 46. <https://doi.org/10.12952/journal.elementa.000046>
- Dugdale, R. C. (1967). Nutrient limitation in the sea: Dynamics, identification, and significance. *Limnology and Oceanography*, 12, 685–695.
- Dunne, J. P., Armstrong, R. A., Gnanadesikan, A., & Sarmiento, J. L. (2005). Empirical and mechanistic models for the particle export ratio. *Global Biogeochemical Cycles*, 19, GB4026. <https://doi.org/10.1029/2004GB002390>
- Duteil, O., Koeve, W., Oschlies, A., Aumont, O., Bianchi, D., Bopp, L., et al. (2012). Preformed and regenerated phosphate in ocean general circulation models: Can right total concentrations be wrong? *Biogeosciences*, 9, 1797–1807. <https://doi.org/10.5194/bg-9-1797-2012>
- Dutkiewicz, S., Scott, J. R., & Follows, M. J. (2013). Winners and losers: Ecological and biogeochemical changes in a warming ocean. *Global Biogeochemical Cycles*, 27, 463–477. <https://doi.org/10.1002/gbc.20042>
- Dyhrman, S. T., Chappell, P. D., Haley, S. T., Moffett, J. W., Orchard, E. D., Waterbury, J. B., et al. (2006). Phosphonate utilization by the globally important marine diazotroph *Trichodesmium*. *Nature*, 439(7072), 68–71. <https://doi.org/10.1038/nature04203>
- Eppley, R. W. (1972). Temperature and phytoplankton growth in the sea. *Fishery Bulletin*, 70(4), 1063–1085.
- Eppley, R. W., Rogers, J. N., & McCarthy, J. J. (1969). Half-saturation constants for uptake of nitrate and ammonium by marine phytoplankton. *Limnology and Oceanography*, 14, 912–920. <https://doi.org/10.4319/lo.1969.14.6.0912>
- Eugster, O., & Gruber, N. (2012). A probabilistic estimate of global marine N-fixation and denitrification. *Global Biogeochemical Cycles*, 26, GB4013. <https://doi.org/10.1029/2012GB004300>
- Falkowski, P., Scholes, R. J., Boyle, E., Canadell, J., Canfield, D., Elser, J., et al. (2000). The global carbon cycle: A test of our knowledge of Earth as a system. *Science*, 290(5490), 291–296. <https://doi.org/10.1126/science.290.5490.291>
- Fleming, R. H. (1940). The composition of plankton and units for reporting population and production. *Proceedings of the sixth Pacific Science Congress California, 1939*, 535–540.
- Flynn, K. J. (2003). Modelling multi-nutrient interactions in phytoplankton; balancing simplicity and realism. *Progress in Oceanography*, 56(2), 249–279. [https://doi.org/10.1016/S0079-6611\(03\)00006-5](https://doi.org/10.1016/S0079-6611(03)00006-5)
- Fraga, F., Rios, A. F., Perez, F. F., & Figueiras, F. G. (1998). Theoretical limits of oxygen : carbon and oxygen : nitrogen ratios during photosynthesis and mineralisation of organic matter in the sea. *Scientia Marina*, 62(1–2), 161–168. <https://doi.org/10.3989/scimar.1998.62n1-2161>
- Francois, R., Honjo, S., Krishfield, R., & Manganini, S. (2002). Factors controlling the flux of organic carbon to the bathypelagic zone of the ocean. *Global Biogeochemical Cycles*, 16(4), 1087. <https://doi.org/10.1029/2001GB001722>
- Friis, K. (2003). The salinity normalization of marine inorganic carbon chemistry data. *Geophysical Research Letters*, 30(2), 1085. <https://doi.org/10.1029/2002GL015898>
- Galbraith, E. D., & Martiny, A. C. (2015). A simple nutrient-dependence mechanism for predicting the stoichiometry of marine ecosystems. *Proceedings of the National Academy of Sciences of the United States of America*, 112, 8199–8204. <https://doi.org/10.1073/pnas.1423917112>
- Galbraith, E. D., Jaccard, S. L., Pedersen, T. F., Sigman, D. M., Haug, G. H., Cook, M., et al. (2007). Carbon dioxide release from the North Pacific abyss during the last deglaciation. *Nature*, 449, 890–893. <https://doi.org/10.1038/nature06227>
- Ganachaud, A. (2003). Large-scale mass transports, water mass formation, and diffusivities estimated from World Ocean Circulation Experiment (WOCE) hydrographic data. *Journal of Geophysical Research*, 108(C7), 3213. <https://doi.org/10.1029/2002JC001565>
- Garcia, H. E., Locarnini, R. A., Boyer, T. P., Antonov, J. I., Mishonov, A. V., Baranova, O. K., et al. (2013). *World Ocean Atlas 2013. Vol. 3: Dissolved oxygen, apparent oxygen utilization, and oxygen saturation* Edited by Levitus, S., & Mishonov Technical, A.: NOAA Atlas NESDIS. 75, p. 27.
- Garcia, H. E., Locarnini, R. A., Boyer, T. P., Antonov, J. I., Baranova, O. K., Zweng, M. M., et al. (2013). *World Ocean Atlas 2013, Volume 4: Dissolved inorganic nutrients (phosphate, nitrate, silicate)* Edited by Levitus, S., & Mishonov Technical, A.: NOAA Atlas NESDIS. 76, p. 25.
- Geider, R., & La Roche, J. (2002). Redfield revisited: Variability of C:N:P in marine microalgae and its biochemical basis. *European Journal of Phycology*, 37(1), 1–17. <https://doi.org/10.1017/S0967026201003456>
- Gotham, I. J., & Rhee, G.-Y. (1981a). Comparative kinetic studies of phosphate-limited growth and phosphate uptake in phytoplankton in continuous culture. *Journal of Phycology*, 17(3), 257–265. <https://doi.org/10.1111/j.1529-8817.1981.tb00848.x>
- Gotham, I. J., & Rhee, G.-Y. (1981b). Comparative kinetic studies of nitrate-limited growth and nitrate uptake in phytoplankton in continuous culture. *Journal of Phycology*, 17(4), 309–314. <https://doi.org/10.1111/j.1529-8817.1981.tb00856.x>
- Gruber, N. (2008). The marine nitrogen cycle: Overview of distributions and processes. In D. G. Capone, D. A. Bronk, M. R. Mulholland, & E. J. Carpenter (Eds.), *Nitrogen in the Marine Environment* (2nd ed., pp. 1–50). Amsterdam: Elsevier.
- Gruber, N., & Sarmiento, J. L. (1997). Global patterns of marine nitrogen fixation and denitrification. *Global Biogeochemical Cycles*, 11(2), 235–266. <https://doi.org/10.1029/97GB00077>
- Hallberg, R. (2013). Using a resolution function to regulate parameterizations of oceanic mesoscale eddy effects. *Ocean Modelling*, 72, 92–103. <https://doi.org/10.1016/j.ocemod.2013.08.007>
- Hedges, J. I., Baldock, J. A., Gélinas, Y., Lee, C., Peterson, M. L., & Wakeham, S. G. (2002). The biochemical and elemental compositions of marine plankton: A NMR perspective. *Marine Chemistry*, 78(1), 47–63. [https://doi.org/10.1016/S0304-4203\(02\)00009-9](https://doi.org/10.1016/S0304-4203(02)00009-9)
- Henson, S. A., Sanders, R., Madsen, E., Morris, P. J., Le Moigne, F., & Quartly, G. D. (2011). A reduced estimate of the strength of the ocean's biological carbon pump. *Geophysical Research Letters*, 38, L04606. <https://doi.org/10.1029/2011GL046735>
- Henson, S. A., Sanders, R., & Madsen, E. (2012). Global patterns in efficiency of particulate organic carbon export and transfer to the deep ocean. *Global Biogeochemical Cycles*, 26, GB1028. <https://doi.org/10.1029/2011GB004099>
- Herrera-Borreguero, L., & Rintoul, S. R. (2011). Subantarctic mode water: Distribution and circulation. *Ocean Dynamics*, 61(1), 103–126. <https://doi.org/10.1007/s10236-010-0352-9>

- Heuzé, C., Heywood, K. J., Stevens, D. P., & Ridley, J. K. (2013). Southern Ocean bottom water characteristics in CMIP5 models. *Geophysical Research Letters*, *40*, 1409–1414. <https://doi.org/10.1002/grl.50287>
- Hirata, T., Hardman-Mountford, N. J., Brewin, R. J. W., Aiken, J., Barlow, R., Suzuki, K., et al. (2011). Synoptic relationships between surface Chlorophyll-a and diagnostic pigments specific to phytoplankton functional types. *Biogeosciences*, *8*(2), 311–327. <https://doi.org/10.5194/bg-8-311-2011>
- Holl, C. M., & Montoya, J. P. (2005). Interactions between nitrate uptake and nitrogen fixation in continuous cultures of the marine diazotroph *Trichodesmium* (Cyanobacteria). *Journal of Phycology*, *41*(6), 1178–1183. <https://doi.org/10.1111/j.1529-8817.2005.00146.x>
- Hunter, J. D. (2007). Matplotlib: A 2D graphics environment. *Computing In Science & Engineering*, *9*(3), 90–95.
- Iudicone, D., Rodgers, K. B., Stendardo, I., Aumont, O., Madec, G., Bopp, L., et al. (2011). Water masses as a unifying framework for understanding the Southern Ocean carbon cycle. *Biogeosciences*, *8*(5), 1031–1052. <https://doi.org/10.5194/bg-8-1031-2011>
- Joos, F. (1999). Global warming and marine carbon cycle feedbacks on future atmospheric CO₂. *Science*, *284*(5413), 464–467. <https://doi.org/10.1126/science.284.5413.464>
- Kalnay, E., Kanamitsu, M., Kistler, R., Collins, W., Deaven, D., Gandin, L., et al. (1996). The NCEP/NCAR 40-year reanalysis project. *Bulletin of the American Meteorological Society*, *77*(3), 437–472. [https://doi.org/10.1175/1520-0477\(1996\)077<0437:TNYRP>2.0.CO;2](https://doi.org/10.1175/1520-0477(1996)077<0437:TNYRP>2.0.CO;2)
- Karl, D. M., & Letelier, R. M. (2008). Nitrogen fixation-enhanced carbon sequestration in low nitrate, low chlorophyll seas. *Marine Ecology Progress Series*, *364*, 257–268. <https://doi.org/10.3354/meps07547>
- Key, R. M., Kozyr, A., Sabine, C. L., Lee, K., Wanninkhof, R., Bullister, J. L., et al. (2004). A global ocean carbon climatology: Results from Global Data Analysis Project (GLODAP). *Global Biogeochemical Cycles*, *18*, GB4031. <https://doi.org/10.1029/2004GB002247>
- Klausmeier, C. A., Litchman, E., Daufresne, T., & Levin, S. A. (2004). Optimal nitrogen-to-phosphorus stoichiometry of phytoplankton. *Nature*, *429*, 171–174. <https://doi.org/10.1029/2001GL014649>
- Kohfeld, K. E., Le Quéré, C., Harrison, S. P., & Anderson, R. F. (2005). Role of marine biology in glacial-interglacial CO₂ cycles. *Science*, *308*(5718), 74–78. <https://doi.org/10.1126/science.1105375>
- Kostadinov, T. S., Siegel, D. A., & Maritorena, S. (2009). Retrieval of the particle size distribution from satellite ocean color observations. *Journal of Geophysical Research*, *114*, C09015. <https://doi.org/10.1029/2009JC005303>
- Kriest, I., & Oschlies, A. (2015). MOPS-1.0: Modelling the regulation of the global oceanic nitrogen budget by marine biogeochemical processes. *Geoscientific Model Development Discussions*, *8*(2), 1945–2010. <https://doi.org/10.5194/gmdd-8-1945-2015>
- Lamarque, J. F., Dentener, F., McConnell, J., Ro, C. U., Shaw, M., Vet, R., et al. (2013). Multi-model mean nitrogen and sulfur deposition from the Atmospheric Chemistry and Climate Model Intercomparison Project (ACCMIP): Evaluation of historical and projected future changes. *Atmospheric Chemistry and Physics*, *13*(16), 7997–8018. <https://doi.org/10.5194/acp-13-7997-2013>
- Landolfi, A., Koeve, W., Dietze, H., Köhler, P., & Oschlies, A. (2015). A new perspective on environmental controls. *Geophysical Research Letters*, *42*, 4482–2289. <https://doi.org/10.1002/2015GL063756>. Abstract
- Laufkötter, C., Vogt, M., Gruber, N., Aumont, O., Bopp, L., Doney, S. C., et al. (2016). Projected decreases in future marine export production: The role of the carbon flux through the upper ocean ecosystem. *Biogeosciences*, *13*(13), 4023–4047. <https://doi.org/10.5194/bg-13-4023-2016>
- Laws, E. A., Falkowski, P. G., Smith, W. O., Ducklow, H., & McCarthy, J. J. (2000). Temperature effects on export production in the open ocean. *Global Biogeochemical Cycles*, *14*(4), 1231–1246. <https://doi.org/10.1029/1999GB001229>
- Le Quéré, C., Harrison, S. P., Colin Prentice, I., Buitenhuis, E. T., Aumont, O., Bopp, L., et al. (2005). Ecosystem dynamics based on plankton functional types for global ocean biogeochemistry models. *Global Change Biology*, *11*, 2016–2040. <https://doi.org/10.1111/j.1365-2486.2005.1004.x>
- Le Quéré, C., Buitenhuis, E. T., Moriarty, R., Alvain, S., Aumont, O., Bopp, L., et al. (2016). Role of zooplankton dynamics for Southern Ocean phytoplankton biomass and global biogeochemical cycles. *Biogeosciences*, *13*(14), 4111–4133. <https://doi.org/10.5194/bg-13-4111-2016>
- Liu, H., Nolla, H., & Campbell, L. (1997). Prochlorococcus growth rate and contribution to primary production in the equatorial and subtropical North Pacific Ocean. *Aquatic Microbial Ecology*, *12*(1), 39–47. <https://doi.org/10.3354/ame012039>
- Locarnini, R. A., Mishonov, A. V., Antonov, J. I., Boyer, T. P., Garcia, H. E., Baranova, O. K., et al. (2013). *World Ocean Atlas 2013, Volume 1: Temperature* Edited by Levitus, S., & Mishonov Technical, A.: NOAA Atlas NESDIS. <https://doi.org/10.1182/blood-2011-06-357442>
- Lumpkin, R., & Speer, K. (2007). Global ocean meridional overturning. *Journal of Physical Oceanography*, *37*(10), 2550–2562. <https://doi.org/10.1175/JPO3130.1>
- Luo, Y.-W., Doney, S. C., Anderson, L. A., Benavides, M., Berman-Frank, I., Bode, A., et al. (2012). Database of diazotrophs in global ocean: Abundance, biomass and nitrogen fixation rates. *Earth System Science Data*, *4*(1), 47–73. <https://doi.org/10.5194/essd-4-47-2012>
- Luo, Y. W., Lima, I. D., Karl, D. M., Deutsch, C. A., & Doney, S. C. (2014). Data-based assessment of environmental controls on global marine nitrogen fixation. *Biogeosciences*, *11*(3), 691–708. <https://doi.org/10.5194/bg-11-691-2014>
- Mahowald, N. M., Baker, A. R., Bergametti, G., Brooks, N., Duce, R. A., Jickells, T. D., et al. (2005). Atmospheric global dust cycle and iron inputs to the ocean. *Global Biogeochemical Cycles*, *19*, GB4025. <https://doi.org/10.1029/2004GB002402>
- Marinov, I., Gnanadesikan, A., Sarmiento, J. L., Toggweiler, J. R., Follows, M., & Mignone, B. K. (2008). Impact of oceanic circulation on biological carbon storage in the ocean and atmospheric p CO₂. *Global Biogeochemical Cycles*, *22*, GB3007. <https://doi.org/10.1029/2007GB002958>
- Mariotti, V., Bopp, L., Tagliabue, A., Kageyama, M., & Swingedouw, D. (2012). Marine productivity response to Heinrich events: A model-data comparison. *Climate of the Past*, *8*(5), 1581–1598. <https://doi.org/10.5194/cp-8-1581-2012>
- Marsay, C. M., Sanders, R. J., Henson, S. A., Pabortsava, K., Achterberg, E. P., & Lampitt, R. S. (2015). Attenuation of sinking particulate organic carbon flux through the mesopelagic ocean. *Proceedings of the National Academy of Sciences of the United States of America*, *112*(4), 1089–1094. <https://doi.org/10.1073/pnas.1415311112>
- Martin, J. H., Knauer, G. A., Karl, D. M., & Broenkow, W. W. (1987). VERTEX: Carbon cycling in the northeast Pacific, Deep Sea Research Part A. *Oceanographic Research Papers*, *34*(2), 267–285. [https://doi.org/10.1016/0198-0149\(87\)90086-0](https://doi.org/10.1016/0198-0149(87)90086-0)
- Martiny, A. C., Pham, C. T. A., Primeau, F. W., Vrugt, J. A., Moore, J. K., Levin, S. A., et al. (2013). Strong latitudinal patterns in the elemental ratios of marine plankton and organic matter. *Nature Geoscience*, *6*(4), 279–283. <https://doi.org/10.1038/ngeo1757>
- Matear, R. J., & Hirst, A. C. (1999). Climate change feedback on the future oceanic CO₂ uptake. *Tellus*, *51*, 722–733. <https://doi.org/10.1034/j.1600-0889.1999.t01-1-00012.x>
- Matear, R. J., & Lenton, A. (2014). Quantifying the impact of ocean acidification on our future climate. *Biogeosciences*, *11*(14), 3965–3983. <https://doi.org/10.5194/bg-11-3965-2014>
- Mayewski, P. A., Rohling, E. E., Stager, J. C., Karlén, W., Maasch, K. A., Meeker, L. D., et al. (2004). Holocene climate variability. *Quaternary Research*, *62*(3), 243–255. <https://doi.org/10.1016/j.yqres.2004.07.001>

- McGillicuddy, D. J. (2014). Do Trichodesmium spp. populations in the North Atlantic export most of the nitrogen they fix? *Global Biogeochemical Cycles*, 28, 103–114. <https://doi.org/10.1002/2013GB004652>
- Menviel, L., Joos, F., & Ritz, S. P. (2012). Simulating atmospheric CO₂, 13C and the marine carbon cycle during the Last Glacial-Interglacial cycle: Possible role for a deepening of the mean remineralization depth and an increase in the oceanic nutrient inventory. *Quaternary Science Reviews*, 56, 46–68. <https://doi.org/10.1016/j.quascirev.2012.09.012>
- Mills, M. M., & Arrigo, K. R. (2010). Magnitude of oceanic nitrogen fixation influenced by the nutrient uptake ratio of phytoplankton. *Nature Geoscience*, 3(6), 412–416. <https://doi.org/10.1038/ngeo856>
- Monod, J., & Wollman, É. (1947). Inhibition of growth and adaptation of enzymes in bacteria infected with bacteriophage. *Annales de l'Institut Pasteur*, 73(10), 937–956.
- Moore, C. M., Mills, M. M., Achterberg, E. P., Geider, R. J., LaRoche, J., Lucas, M. I., et al. (2009). Large-scale distribution of Atlantic nitrogen fixation controlled by iron availability. *Nature Geoscience*, 2(12), 867–871. <https://doi.org/10.1038/ngeo667>
- Moore, J. K., & Doney, S. C. (2007). Iron availability limits the ocean nitrogen inventory stabilizing feedbacks between marine denitrification and nitrogen fixation. *Global Biogeochemical Cycles*, 21, GB2001. <https://doi.org/10.1029/2006GB002762>
- Mouw, C. B., Barnett, A., McKinley, G. A., Gloege, L., & Pilcher, D. (2016). Phytoplankton size impact on export flux in the global ocean. *Global Biogeochemical Cycles*, 30, 1542–1562. <https://doi.org/10.1002/2015GB005355>
- Olli, K. (2015). Unraveling the uncertainty and error propagation in the vertical flux Martin curve. *Progress in Oceanography*, 135, 146–155. <https://doi.org/10.1016/j.poccean.2015.05.016>
- Orr, J. C., Najjar, R. G., Aumont, O., Bopp, L., Bullister, J. L., Danabasoglu, G., et al. (2017). Biogeochemical protocols and diagnostics for the CMIP6 Ocean Model Intercomparison Project (OMIP). *Geoscientific Model Development*, 10(6), 2169–2199. <https://doi.org/10.5194/gmd-10-2169-2017>
- Orsi, A. H., Smethie, W. M., & Bullister, J. L. (2002). On the total input of Antarctic waters to the deep ocean: A preliminary estimate from chlorofluorocarbon measurements. *Journal of Geophysical Research*, 107(C8), 3122. <https://doi.org/10.1029/2001JC000976>
- Paulmier, a., Kriest, I., & Oschlies, A. (2009). Stoichiometries of remineralisation and denitrification in global biogeochemical ocean models. *Biogeosciences*, 6(5), 923–935. <https://doi.org/10.5194/bg-6-923-2009>
- Peng, T.-H., & Broecker, W. S. (1987). C/P ratios in marine detritus. *Global Biogeochemical Cycles*, 1(2), 155–161. <https://doi.org/10.1029/GB0011002p00155>
- Phipps, S. J., Rotstayn, L. D., Gordon, H. B., Roberts, J. L., Hirst, A. C., & Budd, W. F. (2011). The CSIRO Mk3L climate system model version 1.0—Part 1: Description and evaluation. *Geoscientific Model Development*, 4(2), 483–509. <https://doi.org/10.5194/gmd-4-483-2011>
- Phipps, S. J., Rotstayn, L. D., Gordon, H. B., Roberts, J. L., Hirst, A. C., & Budd, W. F. (2012). The CSIRO Mk3L climate system model version 1.0—Part 2: Response to external forcings. *Geoscientific Model Development*, 5(3), 649–682. <https://doi.org/10.5194/gmd-5-649-2012>
- Phipps, S. J., McGregor, H. V., Gergis, J., Gallant, A. J. E., Neukom, R., Stevenson, S., et al. (2013). Paleoclimate data-model comparison and the role of climate forcings over the past 1500 years*. *Journal of Climate*, 26(18), 6915–6936. <https://doi.org/10.1175/JCLI-D-12-00108.1>
- Rasmussen, T. L., Thomsen, E., Troelstra, S. R., Kuijpers, A., & Prins, M. A. (2002). Millennial-scale glacial variability versus Holocene stability: Changes in planktic and benthic foraminifera faunas and ocean circulation in the North Atlantic during the last 60 000 years. *Marine Micropaleontology*, 47(1-2), 143–176. [https://doi.org/10.1016/S0377-8398\(02\)00115-9](https://doi.org/10.1016/S0377-8398(02)00115-9)
- Redfield, A. C. (1963). The influence of organisms on the composition of sea-water. *The Sea*, 2, 26–77.
- Redfield, A. C., Smith, H. P., & Ketchum, B. H. (1937). The cycle of organic phosphorus in the Gulf of Maine. *The Biological Bulletin*, 73(3), 421–443.
- Sallée, J. B., Shuckburgh, E., Bruneau, N., Meijers, A. J. S., Bracegirdle, T. J., & Wang, Z. (2013). Assessment of Southern Ocean mixed-layer depths in CMIP5 models: Historical bias and forcing response. *Journal of Geophysical Research: Oceans*, 118, 1845–1862. <https://doi.org/10.1002/jgrc.20157>
- Sallée, J. B., Shuckburgh, E., Bruneau, N., Meijers, A. J. S., Bracegirdle, T. J., Wang, Z., & Roy, T. (2013). Assessment of Southern Ocean water mass circulation and characteristics in CMIP5 models: Historical bias and forcing response. *Journal of Geophysical Research: Oceans*, 118, 1830–1844. <https://doi.org/10.1002/jgrc.20135>
- Sarmiento, J. L., Hughes, T. M. C., Stouffer, R. J., & Manabe, S. (1998). Simulated response of the ocean carbon cycle to anthropogenic climate warming. *Nature*, 393, 245–249.
- Sarmiento, J. L., Gruber, N., Brzezinski, M. a., & Dunne, J. P. (2004). High-latitude controls of the thermocline nutrients and low latitude biological productivity. *Nature*, 427(6969), 56–60. <https://doi.org/10.1038/nature10605>
- Schmittner, A. (2005). Decline of the marine ecosystem caused by a reduction in the Atlantic overturning circulation. *Nature*, 434(7033), 628–633. <https://doi.org/10.1038/nature03476>
- Schmittner, A., & Somes, C. J. (2016). Complementary constraints from carbon (13C) and nitrogen (15N) isotopes on the glacial ocean's soft-tissue biological pump. *Paleoceanography*, 31, 669–693. <https://doi.org/10.1002/2015PA002905>
- Schmittner, A., Oschlies, A., Matthews, H. D., & Galbraith, E. D. (2008). Future changes in climate, ocean circulation, ecosystems, and biogeochemical cycling simulated for a business-as-usual CO₂ emission scenario until year 4000 AD. *Global Biogeochemical Cycles*, 22, GB1013. <https://doi.org/10.1029/2007GB002953>
- Séférian, R., Bopp, L., Gehlen, M., Orr, J. C., Ethé, C., Cadule, P., et al. (2013). Voldoire Skill assessment of three earth system models with common marine biogeochemistry. *Climate Dynamics*, 40(9-10), 2549–2573. <https://doi.org/10.1007/s00382-012-1362-8>
- Shiozaki, T., Nagata, T., Ijichi, M., & Furuya, K. (2015). Nitrogen fixation and the diazotroph community in the temperate coastal region of the northwestern North Pacific. *Biogeosciences*, 12(15), 4751–4764. <https://doi.org/10.5194/bg-12-4751-2015>
- Sloyan, B. M., & Kamenskovich, I. V. (2007). Simulation of subantarctic mode and Antarctic intermediate waters in climate models. *Journal of Climate*, 20(20), 5061–5080. <https://doi.org/10.1175/JCLI4295.1>
- Smith, R. E. H. (1982). Size-dependent phosphorus uptake kinetics and cell quota in phytoplankton. *Journal of Phycology*, 18, 275–284.
- Smith, S., Yamanaka, Y., Pahlow, M., & Oschlies, A. (2009). Optimal uptake kinetics: Physiological acclimation explains the pattern of nitrate uptake by phytoplankton in the ocean. *Marine Ecology Progress Series*, 384, 1–12. <https://doi.org/10.3354/meps08022>
- Smith, S. L., & Yamanaka, Y. (2007). Optimization-based model of multi-nutrient uptake kinetics. *Limnology and Oceanography*, 52(4), 1545–1558. <https://doi.org/10.1097/EDE.Ob013e318156bfcd>
- Stow, C. A., Jolliff, J., McGillicuddy, D. J., Doney, S. C., Allen, J. I., Friedrichs, M. A., et al. (2009). Skill assessment for coupled biological/physical models of marine systems. *Journal of Marine Systems*, 76(1-2), 4–15. <https://doi.org/10.1016/j.jmarsys.2008.03.011>
- Su, B., Pahlow, M., Wagner, H., & Oschlies, A. (2015). What prevents nitrogen depletion in the oxygen minimum zone of the eastern tropical South Pacific?. *Biogeosciences*, 12(4), 1113–1130. <https://doi.org/10.5194/bg-12-1113-2015>
- Takahashi, T., Broecker, W. S., & Langer, S. (1985). Redfield ratios based on chemical data from isopycnal surfaces. *Journal of Geophysical Research*, 90, 6907–6924.

- Talley, L. (2013). Closure of the global overturning circulation through the Indian, Pacific, and Southern Oceans: Schematics and transports. *Oceanography*, 26(1), 80–97. <https://doi.org/10.5670/oceanog.2013.07>
- Talley, L. D., Reid, J. L., & Robbins, P. E. (2003). Data-based meridional overturning streamfunctions for the global ocean. *Journal of Climate*, 16(19), 3213–3226. [https://doi.org/10.1175/1520-0442\(2003\)016<3213:DMOSFT>2.0.CO;2](https://doi.org/10.1175/1520-0442(2003)016<3213:DMOSFT>2.0.CO;2)
- Tanioka, T., & Matsumoto, K. (2017). Buffering of ocean export production by flexible elemental stoichiometry of particulate organic matter. *Global Biogeochemical Cycles*, 31, 1528–1542. <https://doi.org/10.1002/2017GB005670>
- Taylor, K. E. (2001). Summarizing multiple aspects of model performance in a single diagram. *Journal of Geophysical Research*, 106(D7), 7183–7192. <https://doi.org/10.1029/2000JD900719>
- Taylor, K. E., Stouffer, R. J., & Meehl, G. A. (2012). An overview of CMIP5 and experimental design. *Bulletin of the American Meteorological Society*, 93, 485–498. <https://doi.org/10.1175/BAMS-D-11-00094>
- Thyng, K. M., Greene, C. A., Hetland, R. D., Zimmerle, H. M., & DiMarco, S. F. (2016). True colors of oceanography: Guidelines for effective and accurate colormap selection. *Oceanography*, 29(3), 9–13.
- Timmermans, K. R., Gerringa, L. J. A., Baar, H. J. W. D., Der, B. V., Veldhuis, M. J. W., Jong, J. T. M. D., et al. (2001). Growth rates of large and small Southern Ocean diatoms in relation to availability of iron in natural seawater. *Limnology and Oceanography*, 46(2), 260–266.
- Timmermans, K. R., Wagt, B. V. D., & Baar, H. J. W. D. (2004). Growth rates, half-saturation constants, and silicate, nitrate, and phosphate depletion in relation to iron availability of four large, open-ocean diatoms from the Southern Ocean. *Limnology and Oceanography*, 49(6), 2141–2151. <https://doi.org/10.4319/lo.2004.49.6.2141>
- Voss, M., Dippner, J. W., & Montoya, J. P. (2001). Nitrogen isotope patterns in the oxygen-deficient waters of the eastern tropical North Pacific Ocean. *Deep Sea Research Part I: Oceanographic Research Papers*, 48(8), 1905–1921. [https://doi.org/10.1016/S0967-0637\(00\)00110-2](https://doi.org/10.1016/S0967-0637(00)00110-2)
- Weber, T., & Deutsch, C. (2012). Oceanic nitrogen reservoir regulated by plankton diversity and ocean circulation. *Nature*, 489(7416), 419–22. <https://doi.org/10.1038/nature11357>
- Weber, T., & Deutsch, C. (2014). Local versus basin-scale limitation of marine nitrogen fixation. *Proceedings of the National Academy of Sciences of the United States of America*, 111(24), 8741–8746. <https://doi.org/10.1073/pnas.1317193111>
- Weber, T., Cram, J. A., Leung, S. W., DeVries, T., & Deutsch, C. (2016). Deep ocean nutrients imply large latitudinal variation in particle transfer efficiency. *Proceedings of the National Academy of Sciences of the United States of America*, 113(31), 8606–8611. <https://doi.org/10.1073/pnas.1604414113>
- Weber, T. S., & Deutsch, C. (2010). Ocean nutrient ratios governed by plankton biogeography. *Nature*, 467(7315), 550–4. <https://doi.org/10.1038/nature09403>
- Weeding, B., & Trull, T. W. (2014). Hourly oxygen and total gas tension measurements at the Southern Ocean time series site reveal winter ventilation and spring net community production. *Journal of Geophysical Research: Oceans*, 119, 348–358. <https://doi.org/10.1002/2013JC009302>
- Westberry, T., Behrenfeld, M. J., Siegel, D. A., & Boss, E. (2008). Carbon-based primary productivity modeling with vertically resolved photoacclimation. *Global Biogeochemical Cycles*, 22, GB2024. <https://doi.org/10.1029/2007GB003078>
- Westberry, T. K., & Siegel, D. A. (2006). Spatial and temporal distribution of Trichodesmium blooms in the world's oceans. *Global Biogeochemical Cycles*, 20, GB4016. <https://doi.org/10.1029/2005GB002673>
- Wolf-Gladrow, D. A., Zeebe, R. E., Klaas, C., Körtzinger, A., & Dickson, A. G. (2007). Total alkalinity: The explicit conservative expression and its application to biogeochemical processes. *Marine Chemistry*, 106, 287–300. <https://doi.org/10.1016/j.marchem.2007.01.006>
- Worden, A. Z., Nolan, J. K., & Palenik, B. (2004). Assessing the dynamics and ecology of marine picophytoplankton: The importance of the eukaryotic component. *Limnology and Oceanography*, 49(1), 168–179. <https://doi.org/10.4319/lo.2004.49.1.0168>
- Worden, A. Z., Follows, M. J., Giovannoni, S. J., Wilken, S., Zimmerman, A. E., & Keeling, P. J. (2015). Rethinking the marine carbon cycle: Factoring in the multifarious lifestyles of microbes. *Science*, 347(6223), 1257594. <https://doi.org/10.1126/science.1257594>
- Zweng, M., Reagan, J., Antonov, J., Locarnini, R., Mishonov, A., Boyer, T., et al. (2013). *World Ocean Atlas 2013 volume 2: Salinity* Edited by Levitus, S., & Mishonov Technical, A.: NOAA Atlas NESDIS, 74, p. 39.